Department of Physics and Astronomy

University of Heidelberg

Master thesis

in Physics

submitted by

Antonia Schneider

born in Mannheim

2019

Design of the

Analysis Trap and He Ion Source

for the $^3\text{He}^{2+}$ magnetic moment measurement

This Master thesis has been carried out by Antonia Schneider

at the

Max-Planck-Institut für Kernphysik, Heidelberg

under the supervision of

Herrn Prof. Dr. Klaus Blaum

Design der Analysefalle und He-Ionenquelle für die Bestimmung des magnetischen Kernmoments von ^{3}He

Es wird ein neues Experiment zur ersten direkten Messung des magnetischen Moments von ^{3}He^{2+} und der Hyperfeinstruktur-Aufspaltung von ^{3}He$^+$ konstruiert. Zu diesem Zweck soll die axiale Frequenzverschiebung detektiert werden, die ein Spin-Flip eines einzelnen Helium-Ions in einer inhomogenen Penning-Falle hervorruft. Dies stellt im Fall von ^{3}He^{2+} eine besondere Herausforderung dar, da die im Vergleich zum Proton größere Masse und Ladung sowie das kleinere magnetische Moment ein schlechteres Signal-Rausch-Verhältnis verursachen. Aus diesem Grund wird im ersten Teil dieser Arbeit eine neue Analysefalle entwickelt, die auf die Detektion von Kernspin-Flips optimiert ist. Im zweiten Teil wird eine interne Heliumquelle konstruiert und dazu zwei mögliche Designs getestet: ein He-beladenes Titanfilament und eine He-gefüllte Kugel aus Quarzglas. Diese werden erhitzt um Heliumatome freizugeben. Der Heliumgehalt der beladenen Titanproben wurde mit einem Edelgas-Spektrometer gemessen. Die Proben enthalten nach dem Laden ausreichend Helium, verlieren allerdings 90 % des Heliumgehalts in zwei Monaten. Die Quarzkugel wurde in einem Testaufbau mit einer Penning-Falle untersucht, wo nach Erhitzen der Kugel ^{3}He$^+$ Ionen nachgewiesen werden konnten.

Design of the Analysis Trap and He Ion Source for the ^{3}He nuclear magnetic moment measurement

A new experiment for the first direct measurement of the ^{3}He^{2+} nuclear magnetic moment and the ^{3}He$^+$ hyperfine splitting is being constructed. To this end, the axial frequency shift caused by a spin-flip of a single helium ion in an inhomogeneous Penning trap is to be detected. This poses a particular challenge in case of ^{3}He^{2+} as the compared to a proton larger mass and charge as well as the smaller magnetic moment correspond to a reduced signal-to noise ratio. Therefore, a new analysis trap optimized for nuclear spin-flip detection is developed in the first part of this thesis. In the second part, an internal source of ^{3}He is constructed and two possible designs tested: a He-loaded titanium filament and a He-filled fused silica sphere, which are heated to release ^{3}He atoms. The helium content of the loaded titanium samples are measured using a noble gas spectrometer. While the samples contained a sufficient amount of helium after loading, they are found to leak 90 % of their helium content in two months. The fused silica sphere is tested in a Penning trap test setup, where ^{3}He$^+$ ions were detected after heating the sphere.

Contents

1 Motivation

Recent advances in quantum-jump spectroscopy of single isolated nucleons in a Penning trap led to most precise measurements of the nuclear magnetic moments of the proton and antiproton [1, 2]. Based on these successes we construct a new experiment aiming at the first direct high-precision measurement of the ^{3}He^{2+} nuclear magnetic moment μ_{He} with a relative precision of 10^{-9} or better as well as an improved value for the ground state hyperfine splitting of ^{3}He$^+$ by at least a factor of 10 with a relative precision of 0.1 ppb.

1.1 Helium NMR Probes

So far, only indirect determinations of μ_{He} exist, which compare the nuclear magnetic resonance (NMR) frequency of ^{3}He to water or molecular hydrogen NMR frequencies [3, 4, 5]. These allow for a relative precision of 12 ppb, only, limited by the systematic effects in water NMR probes discussed below. The direct high-precision determination of μ_{He} which we are aiming for will establish ^{3}He NMR probes as an independent standard for absolute precision magnetometry.

Unlike SQUIDs, NMR probes allow high-precision measurements of not only magnetic field fluctuations but also the absolute magnetic field and compared to optical magnetometers, NMR probes lack the poorly defined blend of hyperfine lines [6]. Helium NMR probes, in particular, offer a much higher accuracy than water NMR probes due to their reduced dependence on impurities, probe shape and environmental influences such as temperature, pressure, or chemical corrections [7, 8]. Furthermore, the diamagnetic shielding parameter σ is known more precisely for ^{3}He than water. The diamagnetic shielding of the bare nuclear magnetic moment caused by the electrons surrounding the nucleus changes the NMR resonance frequency by a factor of $1 - \sigma$. For ^{3}He, this factor does not have to be calibrated by a set of dependent measurements as for water but is known by theory to a fractional accuracy of 10^{-10} [9]. However, so far ^{3}He NMR probes lack a calibration by a direct measurement of the nuclear magnetic moment independent of water NMR probes.

In addition, a direct measurement of μ_{He} allows for the first test of theoretical diamagnetic shielding corrections of NMR probes. The ratio of the molecular hydrogen and ^{3}He shielding parameters is

$$\frac{1 - \sigma_{H_2}}{1 - \sigma_{He}} = \frac{\nu'_{H_2}}{\nu'_{He}} \frac{\mu_{He}}{\mu_p}. \tag{1.1}$$

Here, ν'_{H_2} and ν'_{He} are the nuclear resonance frequencies of molecular hydrogen and atomic ^{3}He, i.e. including electronic shielding. The ratio of these frequencies is

known to 3 ppb [4] and the proton magnetic moment μ_p has been directly determined with 300 ppt precision [1]. Therefore, an independent measurement of μ_{He} with ppb precision makes it possible to test the theoretical value of the shielding parameter ratio with ppb precision.

In [10], a $5 \cdot 10^{-8}$ discrepancy is observed between two values for the atomic hydrogen shielding σ_H. The first value was determined via the resonance frequency difference (chemical shift) compared to molecular hydrogen and the accepted σ_{H_2} reference and the second was determined from the bare magnetic moments of the proton and $^3\text{He}^{2+}$ as in Eq. (1.1). This discrepancy could be caused either by a 10^{-7} shift in μ_{He} or an inaccuracy in the reference molecular hydrogen shielding parameter. The result of this experiment will provide independent and definite impact to ultimately pin-down the current uncertainty.

1.2 Muon g-2 Determination

Motivated by the 3σ discrepancy between experimental and theoretical values of the muon's anomalous magnetic moment a_μ as predicted by the Standard Model, two experiments located at Fermilab and J-Parc [11, 12] aim at an improved measurement with a precision of 140 ppb. Although pursuing conceptually different approaches, both experiments plan to determine a_μ from the measurement of two frequencies. These frequencies are the anomaly frequency ω_a of the muon in a precisely tuned magnetic field [13] and the spin precession frequency ω'_p of nucleons in state-of-the-art water NMR probes to measure the magnetic field. Here, careful characterizations of a chain of NMR probes are carried out to enable the challenging precision measurement of the magnetic field [14]. The successful implementation of our experiment would enable an uncorrelated and independent magnetic field measurement with very different and smaller systematic effects, once μ_{He} has been measured directly and independent from water. The current approach to determine a_μ employs the relation:

$$a_\mu = \frac{\omega_a/\omega'_p}{\mu_\mu/\mu'_p - \omega_a/\omega'_p}. \tag{1.2}$$

All quantities on the right hand side of Eq. (1.2) are determined experimentally, however, the experimental uncertainty in the magnetic moment ratio μ_μ/μ'_p is at a level of 120 ppb. Therefore, an alternative determination of a_μ without the factor μ_μ/μ'_p is appealing. This can be achieved by expressing a_μ as

$$a_\mu = \frac{g_e}{2} \frac{\omega_a}{\omega'_{NMR}} \frac{m_\mu}{m_e} \frac{\mu'_{NMR}}{\mu_e}, \tag{1.3}$$

where m_μ/m_e is the muon-to-electron mass ratio and g_e is the electron g-factor, which are known to 25 ppb and 0.76 ppt, respectively [15, 16]. While this approach is also applicable with water NMR probes, ^3He probes offer reduced systematic

uncertainties as described in the last section. Considering a ^{3}He probe, the last factor in Eq. (1.3), which is the electron to water NMR magnetic moment ratio, can be rewritten as

$$\frac{\mu'_{He}}{\mu_e} = \frac{m_u}{m_{He}}\frac{m_e}{m_u}\frac{1}{g_e}(1 - \sigma_{He})\frac{4\mu_{He}m_{He}}{e\hbar}. \tag{1.4}$$

Here, m_u is the atomic mass unit so that the first two factors above are known to 14 ppt and 30 ppt [17, 18]. The last factor in Eq. (1.4) is exactly equal to the ratio of the Larmor frequency ω_L and the cyclotron frequency ω_c of the ^{3}He ion

$$\frac{\omega_L}{\omega_c} = \mu_{He}\left(\frac{q\hbar}{2m_{He}}\right)^{-1}. \tag{1.5}$$

In our experiment we plan to measure both frequencies directly in a Penning trap with 1 ppb precision. This will make it possible to use the determination of a_μ with ^{3}He NMR probes as an uncorrelated test of the results with water NMR probes.

Note that the mass ratio m_μ/m_e in Eq. (1.3) is calculated from the measured ground state hyperfine interval in muonium $\Delta\nu_{Mu}$ [15] using Standard Model theory, so that potential new physics contributions in a_μ have to also be included in the hyperfine interval $\Delta\nu_{Mu}$ for consistency.

1.3 Hyperfine Splitting

Currently, the most precise measurement of the zero-field ground state hyperfine splitting of ^{3}He$^+$ studies the spin-dependent collision processes between a cloud of ^{3}He$^+$ ions stored in a radio-frequency quadrupole ion trap and a polarized beam of Cs atoms [19]. This measurement is limited by resonance line broadening due to the second order Doppler effect in the used room temperature apparatus to a relative precision of 10^{-9}. For hydrogen-like systems the hyperfine splitting is given to leading order by the Fermi contact term E_F [20], which accounts for the interaction of the nuclear and electronic magnetic moments. Corrections contributing to the energy spitting arise from QED effects δ_{QED}, the strong interaction δ_{hvp} and recoil effects δ_{rec}. In addition the nuclear polarizability as well as the spatial distribution of the charge and the magnetic moment within the nucleus δ_{nucl}, the latter known as Zeemach radius, contribute:

$$\Delta E_{\text{HFS}} = E_F(1 + \delta_{\text{QED}} + \delta_{\text{rec}} + \delta_{\text{hvp}} + \delta_{\text{nucl}}). \tag{1.6}$$

The measurement of ΔE_{HFS} we are aiming for is highly sensitive to nuclear structure effects, as δ_{nucl} contributes at a relative precision of $2 \cdot 10^{-4}$.

2 Theoretical Basics

2.1 Ideal Penning Trap

An ideal Penning trap consists of a homogeneous magnetic field $\vec{B} = B_0 \vec{e_z}$ in the axial direction and a superimposed quadrupolar electrostatic potential

$$V(z, \rho) = V_0 C_2 \left(z^2 - \frac{\rho^2}{2} \right). \tag{2.1}$$

Here, V_0 is the trapping voltage and C_2 characterizes the typical geometrical length scale of the potential.

The electrostatic force $\vec{F_E} = -q\vec{\nabla}V$, acting on the trapped particle of mass m and charge q, leads to a harmonic oscillation in the axial direction with frequency

$$\omega_z = \sqrt{2\frac{q}{m}C_2 V_0}. \tag{2.2}$$

Additionally, the magnetic field confines the ion in the radial direction via the Lorentz force $\vec{F_L} = q\vec{v} \times \vec{B}$. Solving the equation of motion for the total force $\vec{F} = \vec{F_E} + \vec{F_L}$ leads to the eigenfrequencies

$$\omega_\pm = \frac{1}{2}\left(\omega_c \pm \sqrt{\omega_c^2 - 2\omega_z^2} \right), \tag{2.3}$$

termed magnetron frequency ω_- and modified cyclotron frequency ω_+. Here, ω_c is the so-called free cyclotron frequency

$$\omega_c = \frac{q}{m}B_0. \tag{2.4}$$

In practice, the optimal electrostatic potential given in Eq. (2.1) can be created with a stack of cylindrical electrodes. A five-electrode Penning trap consists of a central ring electrode at voltage V_0, two neighboring correction electrodes with voltage V_c and two endcaps connected to ground. The ratio of the ring voltage and correction voltage is called the tuning ratio

$$TR = \frac{V_c}{V_0}. \tag{2.5}$$

Choosing adequate electrode lengths, the Penning trap can be designed to be "compensated" as well as "orthogonal".

- Orthogonality means that the axial frequency ν_z of the particle is independent of the voltage applied to the correction electrodes, i.e. $D_2 = 0$ with

$$D_2 = \frac{\partial \nu_z}{\partial TR} = \frac{\nu_z}{2C_2} d_2 \tag{2.6}$$

where $d_2 = \frac{\partial C_2}{\partial TR}$.

- Compensation means that the first higher order corrections C_4 and C_6 of the multipolar potential expansion along the z-axis

$$V(z) = \sum_n C_n z^n \tag{2.7}$$

vanish at the same tuning ratio. Residual unharmonicities lead to unwanted shifts of the axial resonance frequency that depend on the energy $E_z = m\omega_z^2\langle z^2\rangle$:

$$\Delta\nu_{z,4} = \nu_z \frac{3}{4}\frac{C_4}{C_2^2}\frac{E_z}{qV_0}, \tag{2.8}$$

$$\Delta\nu_{z,6} = \nu_z \frac{15}{16}\left(\frac{E_z}{qV_0}\right)^2 \frac{C_6}{C_2^3}, \tag{2.9}$$

$$\Delta\nu_{z,8} = \nu_z \frac{35}{32}\left(\frac{E_z}{qV_0}\right)^3 \frac{C_8}{C_2^4}. \tag{2.10}$$

2.2 Determination of the g-Factor

The helion $^3\text{He}^{2+}$ has a nuclear spin $I = \frac{1}{2}$ and an associated magnetic moment

$$\vec{\mu_I} = g_I \mu_N \frac{\vec{I}}{\hbar}, \tag{2.11}$$

with the nuclear g-factor g_I, the reduced Planck constant $\hbar$ and the nuclear magneton $\mu_N = e\hbar/(2m_{\text{He}})$. It follows that in the magnetic field $\vec{B} = \vec{e_z}B_0$ the spin states $m_I = \pm\frac{1}{2}$ are separated by the energy difference

$$g_I\mu_N B_0 = 2\mu_I B_0 \tag{2.12}$$
$$= \hbar\omega_L, \tag{2.13}$$
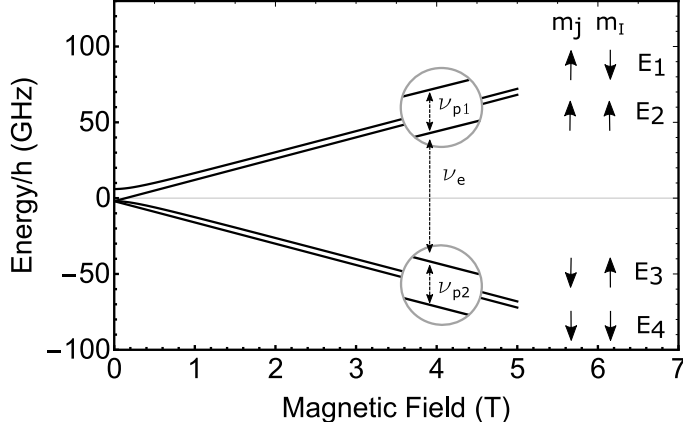
which defines the Larmor frequency ω_L.

Figure 2.1: Zeeman effect of the ground-state hyperfine splitting in $^3\mathrm{He}^+$. The relevant transitions are indicated by $\nu_{p1/2}$ and ν_e.

Thus, the ratio of Larmor frequency to cyclotron frequency

$$\frac{\omega_L}{\omega_c} = \mu_I \left(\frac{q\hbar}{2m_{\mathrm{He}}}\right)^{-1} = g\frac{m_{\mathrm{He}}}{2m_p}\frac{e}{q} = g\frac{m_{\mathrm{He}}}{4m_p} \tag{2.14}$$

gives the g-factor in dependence of the helium-to-proton mass ratio m_{He}/m_p or the magnetic moment in units of $q\hbar/(2m_{\mathrm{He}})$.

The singly charged helium-3 ion $^3\mathrm{He}^+$ has a nuclear spin $I = \frac{1}{2}$ and an electron angular momentum in the ground state $J = \frac{1}{2}$. The spin-flip transition frequencies of either the electron (ν_e in Fig. 2.1) or the nucleus (ν_{p1} and ν_{p2} in Fig. 2.1) can be measured in order to determine the electronic and the nuclear g-factors, as well as the hyperfine splitting ΔE_{HFS} in Eq. (1.6).

2.2.1 Measurement Scheme

While ω_c follows from the ion's eigenmotions which in turn can be detected via the image charges they induce in the trap electrodes, the Larmor frequency is not accompanied by a motion. As explained in the next section, the spin transition frequency can be measured using a strong magnetic inhomogeneity, which leads to energy dependent shifts of the ion's eigenfrequencies. For this reason the eigenfrequencies are measured in the homogeneous field of the precision trap whereas the spin-flip detection is performed in a separate trap, the analysis trap. The trap stack, see Fig. 2.2, also includes a cooling trap, where $^9\mathrm{Be}^+$ ions are laser-cooled, and a coupling trap, where the $^3\mathrm{He}$ ions can be sympathetically cooled via image currents induced in the shared electrode of both traps (common endcap technique) [21]. A measurement cycle proceeds by the following steps:

- A single $^3\mathrm{He}^{2+}$ ion in the coupling trap and a cloud of $^9\mathrm{Be}^+$ ions in the cooling trap are tuned into resonance with each other.
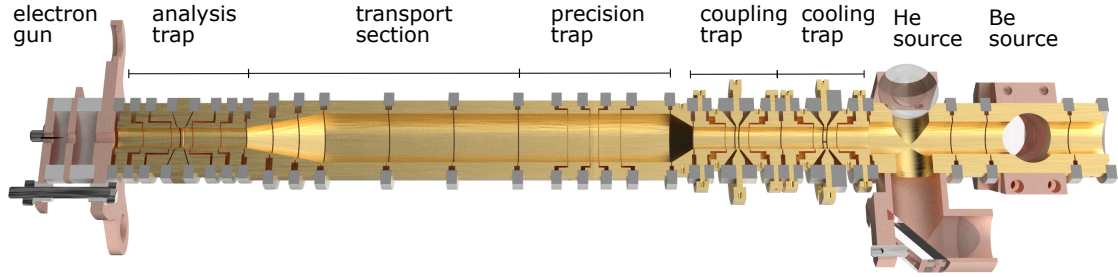
Figure 2.2: Trap assembly as planned for the nuclear magnetic moment measurement of ^{3}He. It includes four Penning traps, the analysis trap, the precision trap, the cooling trap and the coupling trap. Atoms from the ^{3}He and ^{9}Be source are ionized by electrons emitted from the field emission point in the electron gun.

- Laser cooling of the axial mode of the Be-ion cloud to the Doppler limit.

- The axial mode of the He ion is sympathetically cooled. The cyclotron mode of the He ion is cooled by coupling the axial and cyclotron mode at the respective lower sideband.

- The He ion is transported to the analysis trap where the initial spin state is detected.

- The He ion is transported to the precision trap, where the cyclotron frequency of the helium ion is measured while spin flips at the Larmor frequency are driven.

- Re-cooling of the cyclotron mode in the coupling trap.

- Detection of final spin state in the analysis trap.

This scheme is repeated with different spin-flip drive frequencies to obtain the spin-flip probability as function of the ratio of the drive frequency ν_L and the cyclotron frequency ν_c.

2.3 Magnetic Bottle

In the analysis trap the spin state is determined via the continuous Stern-Gerlach effect, i.e. the coupling of the spin magnetic moment to the axial frequency. To this purpose a so called magnetic bottle B_2 is superimposed on the homogeneous magnetic field resulting in the total magnetic field

$$\vec{B}(z,\rho) = B_0 \vec{e_z} + B_2 \left(\left(z^2 - \frac{\rho^2}{2} \right) \vec{e_z} - \rho z \vec{e_\rho} \right). \tag{2.15}$$

This leads to an additional term $\Delta E = -\vec{\mu} \cdot \vec{B}$ in the effective potential, so that at radius $\rho = 0$ the modified equation of motion in the axial direction becomes

$$m_{\mathrm{He}}\ddot{z} = -(\omega_z^2 + 2B_2\mu_z)z. \tag{2.16}$$

Here, μ_z is the z-component of the ion's magnetic moment. Thus, the axial frequency is shifted by

$$\Delta\omega_z = \left(\sqrt{1 + \frac{2B_2\mu_z}{\omega_z^2}} - 1\right)\omega_z \approx \frac{B_2}{\omega_z}\frac{\mu_z}{m_{\mathrm{He}}} \tag{2.17}$$

$$\Leftrightarrow \Delta\nu_z = \frac{B_2}{4\pi^2\nu_z}\frac{\mu_z}{m_{\mathrm{He}}}. \tag{2.18}$$

The ion's magnetic moment $\vec{\mu} = \vec{\mu_s} + \vec{\mu_+} + \vec{\mu_-}$ consists of the contributions from the spin and the two orbital angular momenta. μ_+ and μ_- are the magnetic moments corresponding to the cyclotron and magnetron motion, respectively. It follows the z-component of the magnetic moment

$$\mu_z = \mu_{z,s} + \mu_{z,+} + \mu_{z,-}. \tag{2.19}$$

Viewing the two radial modes as one-dimensional quantum harmonic oscillators with quantum number $n_\pm$ and energy $E_\pm = h\nu_\pm(n_\pm + \frac{1}{2})$, one obtains the axial frequency shift

$$\Delta\nu_{z,\pm} = \frac{h\nu_\pm}{4\pi^2 m_{\mathrm{He}}\nu_z}\frac{B_2}{B_0}(n_\pm + \frac{1}{2}) \tag{2.20}$$

by inserting $\mu_{z,\pm} = \frac{E_\pm}{B_0}$ into Eq. (2.18). In case of a spin-flip $\Delta m_s = \pm 1$ it follows from Eq. (2.18) and Eq. (2.13)

$$\Delta\nu_{\mathrm{z,SF}} = \pm\frac{h\nu_L}{4\pi^2 m_{\mathrm{He}}\nu_z}\frac{B_2}{B_0} = \pm\frac{\mu_I}{2\pi^2 m_{\mathrm{He}}\nu_z}B_2. \tag{2.21}$$

Inserting Eq. (2.2) gives

$$\Delta\nu_{\mathrm{z,SF}} = \frac{1}{\sqrt{2}\pi}\sqrt{\frac{1}{qm_{\mathrm{He}}}}\mu_I\frac{B_2}{\sqrt{C_2 V_0}} \tag{2.22}$$

in terms of the trap parameters B_2 and C_2, which can be optimized to maximize $\Delta\nu_{\mathrm{z,SF}}$. Thus, a spin-flip is detectable via the resulting change of the axial frequency, while changes in the radial modes cause unwanted noise on this signal, as described in the following.

2.4 Cyclotron noise

The axial frequency shift $\Delta\nu_{\text{z,SF}}$ due to a spin-flip can only be distinguished if the axial frequency is otherwise sufficiently stable. However, broadband voltage noise causes quantum number fluctuations in the radial modes which lead to axial frequency fluctuations according to Eq. (2.20). Here, the main contribution comes from the cyclotron mode, as the modified cyclotron frequency is much larger than the magnetron frequency $\nu_+ \gg \nu_-$.

The voltage noise S_V on the electrodes causes a transition rate [22, 23]

$$\frac{\partial n_+}{\partial t} = \frac{q^2 n_+}{2m_{\text{He}}\hbar\omega_+}\Lambda^2 S_V(\omega_+) \tag{2.23}$$

in the cyclotron mode. Here,

$$\Lambda^2 = \sum_{n=1}^{5}\left(\frac{\partial\Phi_n}{\partial\rho}\right)^2 \tag{2.24}$$

depends on the radial gradient of the electrostatic potentials Φ_n of the five electrodes and is therefore a trap specific parameter. The transition rate in Eq. (2.23) corresponds to fluctuations of the axial frequency

$$\sigma_{z,+} = \Delta\nu_{z,+}\sqrt{\frac{\partial n_+}{\partial t}\tau} \propto \sqrt{E_+\tau}\sqrt{\frac{q^3}{m_{\text{He}}}}\frac{B_2}{B_0\nu_z}\Lambda \tag{2.25}$$

at cyclotron energy $E_+ = \hbar\omega_+(n_+ + 1/2)$ and averaging time τ.

As described by Eq. (2.25), the axial frequency noise induced by cyclotron quantum transitions can be suppressed by reducing the cyclotron energy E_+. For this purpose, the trapped $^3\text{He}^{2+}$ ion will be deterministicly cooled in our experiment by sympathetic coupling using a common endcap technique, as described above. From this quasi-deterministic cooling scheme a considerable reduction in experimental cycle times and a high-fidelity spin state detection are expected.

3 Analysis Trap Design

The probability that a spin-flip is correctly identified from a series of axial frequency measurements depends on the signal $\Delta\nu_{z,SF}$ and the axial frequency noise σ_z. Measurements of the axial frequency noise with a proton in a Penning trap [24] are plotted as function of the averaging time in Fig. 3.1. The total noise

$$\sigma_z = \sqrt{\sigma_{z,+}^2 + \sigma_0^2} \tag{3.1}$$

consists of the cyclotron noise component $\sigma_{z,+} \propto \tau^{1/2}$ and a white noise component $\sigma_0 \propto \tau^{-1/2}$. The white noise component is mostly due to FFT averaging, as the axial frequencies are obtained from the FFT spectrum of the image-current signal from the trapped particle. Another source of the white noise are voltage fluctuations that correspond to frequency fluctuations via Eq. (2.2) [2].

Estimating a white noise of $\sigma_0 = 35$ mHz at averaging time $\tau = 200$ s from these measurements, the spin-flip detection fidelity [26, 27] can be calculated as function of the cyclotron energy, see Fig. 3.2 (a). Here, the spin-flip fidelity of a ^{3}He nucleus is compared to that of a proton in the same trap, which is described in [25]. The helion's larger charge and mass increase the cyclotron noise $\sigma_{z,+} \propto \sqrt{q^3/m}$ by a factor of 1.6 compared to the proton, which, however, only affects the fidelity at high cyclotron energies $E_+/k_B > 1$ K. The red dashed line indicates the cyclotron energy which can be reached with laser-cooling in our experiment, showing that at the relevant energy the effect of the cyclotron noise on the fidelity is negligible. This is due to the large magnetic background field $B_0 = 5$ T, which suppresses the cyclotron noise according to Eq. (2.25). At given white noise σ_0, which is independent of B_2 and E_+, the fidelity with laser-cooling depends only on the spin-flip frequency shift $\Delta\nu_{z,SF}$ and is thus significantly smaller for a He ion compared to a proton in the same trap (Fig. 3.2 (b)). As seen from Eq. (2.22), both the larger charge and mass as well as the smaller magnetic moment of a ^{3}He nucleus compared to a proton suppress the spin-flip frequency shift $\Delta\nu_{z,SF} \propto \mu_I/\sqrt{mq}$.

For this reason, a new analysis trap is designed that maximizes $\Delta\nu_{z,SF}$ (section 3.1). With the new design (green solid line in Fig. 3.2), a fidelity of 86 % is reached at $\sigma_0 = 35$ mHz and can be further improved by choosing a larger averaging time, reducing the white noise $\sigma_0 \propto \tau^{-1/2}$. Also, a new trap design is introduced by which cyclotron noise can be suppressed, particularly interesting for experiments without laser-cooling (section 3.2). A similar design was originally proposed as an upgrade of the BASE experiment [28] at CERN. In section 3.6 a second trap design is introduced which aims at further increasing the spin-flip frequency shift by reducing the axial frequency at a given ring voltage.
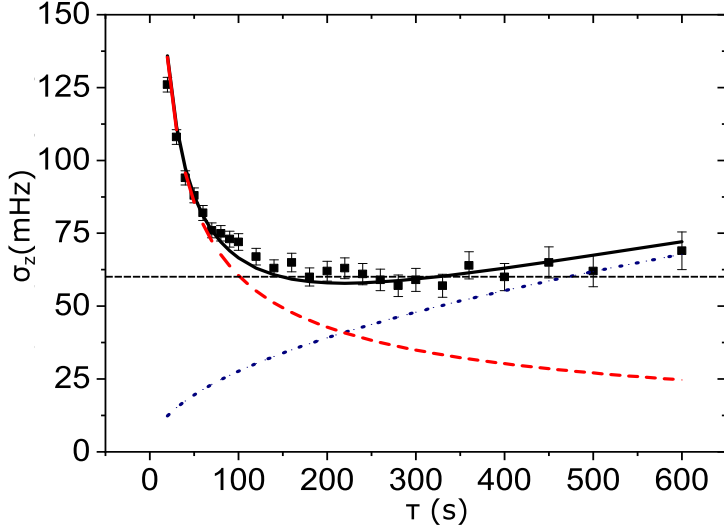
Figure 3.1: Measurement [24] of the axial frequency stability (Allan deviation) of a proton as a function of the averaging time τ. The decreasing red dashed line is the white noise component $\sigma_0 \propto \tau^{-1/2}$ and the blue dotted line is the cyclotron noise $\sigma_c \propto \tau^{1/2}$. The horizontal black dashed line indicates the spin-flip frequency shift $\Delta\nu_{z,\mathrm{SF}}$ of a $^3\mathrm{He}^{2+}$ ion in the same analysis trap described in [25].
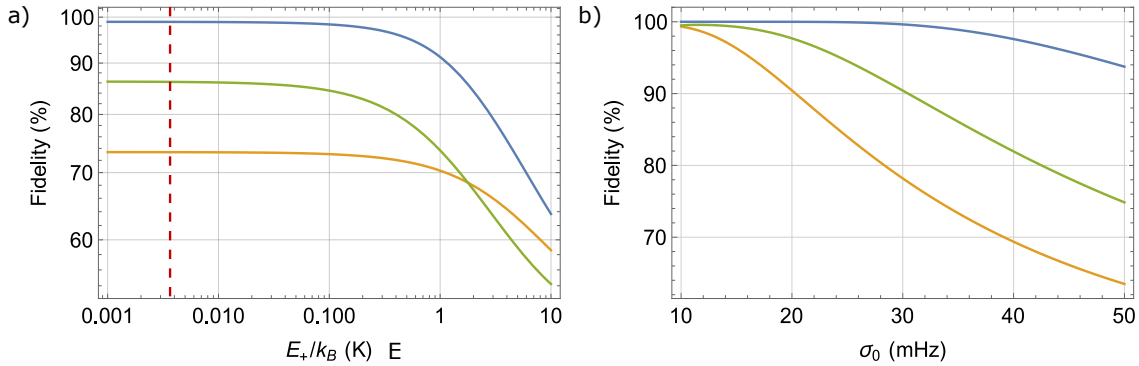

Figure 3.2: Spin-flip detection fidelity of $^3\mathrm{He}^{2+}$ (yellow) compared to a proton (blue) using the Penning trap described in [25] and for a $^3\mathrm{He}^{2+}$ ion in the newly designed trap (green). The magnetic background field is $B_0 = 5$ T. (a) Fidelity as a function of the cyclotron energy E_+ in units of the Boltzmann constant k_B. The red dashed line at $E_+/k_B = 0.01$ K indicates the approximate energy that can be achieved in our experiment through laser-cooling. This calculation assumes white noise of $\sigma_0 = 35$ mHz at averaging time $\tau = 200$ s. (b) Fidelity at cyclotron energy $E_+/k_B = 0.01$ K as function of the white noise σ_0.

15

3.1 Trap Radius

The spin-flip frequency shift is maximized by choosing a small trap radius of only $a = 1.25$ mm. Bringing the ferromagnetic electrodes closer to the ion increases the magnetic bottle B_2 and thus the spin-flip frequency shift $\nu_{z,SF} \propto B_2/\nu_z$. However, a smaller radius also increases the geometrical factor C_2 in Eq. (2.2) and thereby the axial frequency ν_z. This can be counteracted with an accordingly smaller ring voltage V_0, which, however, needs to remain significantly larger than patch potentials of typically a few 10 mV [29]. Therefore, a constant ring voltage $V_0 = -0.8$ V is assumed to test the effect of reducing the radius on the signal $\Delta\nu_{z,SF}$, see Fig. 3.3. Here, $\Delta\nu_{z,SF}$ is calculated using FEM-calculations of the magnetic and electrostatic fields of the proton analysis trap [25] with different trap radii. The electrode lengths were adapted to optimize the electrostatic potential at different radii, as described in section 3.4.
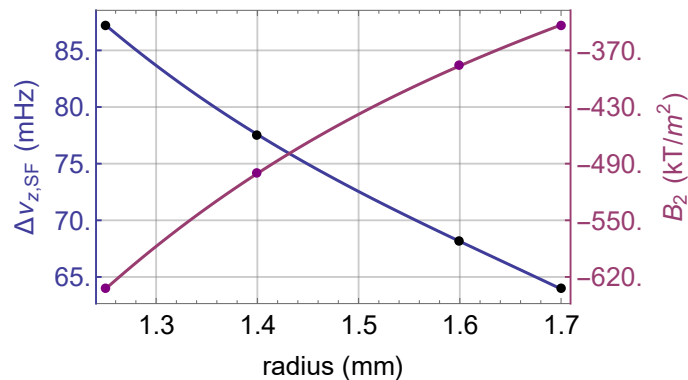

Figure 3.3: Axial frequency shift $\Delta\nu_{z,SF}$ due to a nuclear spin-flip at constant ring voltage V_0 and magnetic bottle B_2 as function of the analysis trap radius. Here, $V_0 = -0.8$ V is assumed.

The results in Fig. 3.3 show that the magnetic bottle scales stronger with the analysis trap radius than the axial frequency. Reducing the radius from 1.8 mm to $a = 1.25$ mm doubles B_2 and increases $\Delta\nu_{z,SF}$ by 150 %. Thus, 90 mHz instead of 60 mHz are reached, leading to the improved spin-flip detection fidelity [26] depicted in Fig. 3.2.

On the other hand, bringing the electrodes closer to the ion will also increase the axial frequency noise induced by cyclotron quantum transitions. The axial frequency shift in case of a cyclotron transition scales with $\Delta\nu_{z,+} \propto B_2/\nu_z$ as does $\Delta\nu_{z,SF}$. Thus, the ratio of the signal to the cyclotron noise is unaffected by the increased magnetic bottle. However, assuming that the quantum jumps causing the cyclotron noise are induced by voltage fluctuations on the electrodes, the cyclotron quantum jump rate will increase if the electrodes are positioned closer to the ion. This is expressed in the geometrical factor Λ in Eq. (2.23). Calculating this parameter at radius 1.8 mm and 1.25 mm via Eq. (2.24) shows an increase of the geometrical
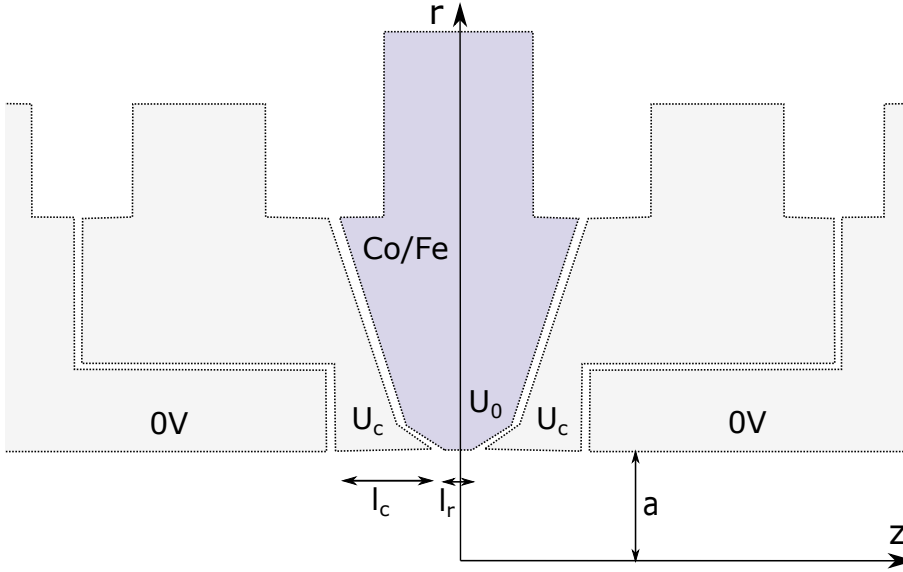
Figure 3.4: Sectional view of the proton analysis trap from [31]. The ferromagnetic ring electrode is displayed in blue. l_r and l_c are the ring length and correction electrode length, respectively.

factor by a factor of $\Lambda(1.25)/\Lambda(1.8) = 1.7$. This effect is mitigated with a novel approach to suppress cyclotron noise, which is described in the next section.

3.2 Ferromagnetic Electrodes

The magnetic bottle B_2 is generated by electrodes made of strong ferromagnetic material. Because of its large saturation magnetization of $M = 187 \mathrm{\,A\,m^{-1}}$, i.e. saturation flux of 2.35 T, a cobalt iron alloy (VACOFLUX 50[30]) is used.

In [31], the analysis trap shown in Fig. 3.4 was designed for proton spin-flip detection with a ferromagnetic ring electrode that creates $B_2 = 300 \mathrm{\,kT\,m^{-2}}$ at a trap radius of $a = 1.8$ mm. This strong magnetic bottle leads to a detectable spin-flip frequency-shift but also reduces the magnetic field at the trap center by $\Delta B_0 \approx -0.8$ T.

According to Eq. (2.25), one possibility to minimize the cyclotron noise is to maximize the magnetic field in the analysis trap center B_0. However, so far, analysis traps were constructed with a ring electrode made of Co/Fe [2, 1, 32, 16, 18]. As depicted in Fig. 3.5, this creates a negative ΔB_0 in the center of the analysis trap. If instead the correction electrodes and endcaps are made from ferromagnetic material, a magnetic field larger than the background field B_0 can be achieved. The comparison is depicted in Fig. 3.5 at radius $a = 1.25$ mm. The ferromagnetic correction electrodes change the magnetic field at the trap center by $\Delta B_0 = 0.4$ T compared to $\Delta B_0 = -0.9$ T in case a ferromagnetic Co/Fe ring electrode is used.

With a background field of 5 T, this leads to an increase by a factor of 1.3 in
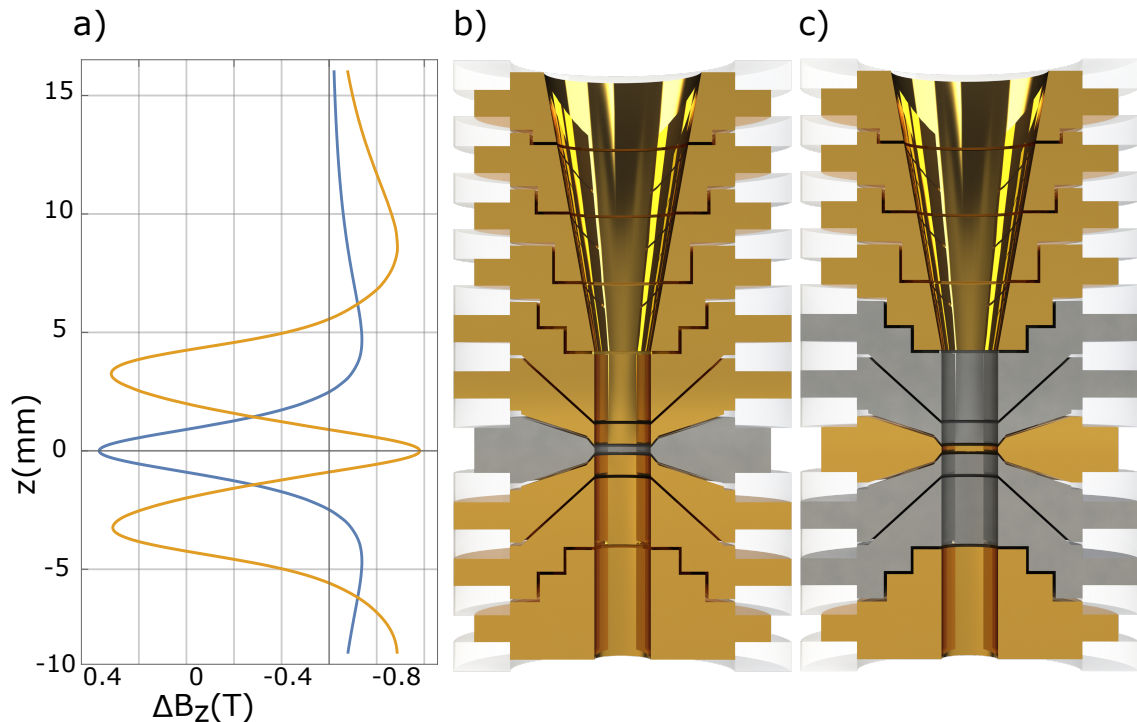
Figure 3.5: (a) Blue solid line: magnetic field of the analysis trap shown in (b), where the ring electrode is made from ferromagnetic Co/Fe. Yellow solid line: magnetic field of the same trap with ferromagnetic correction electrodes and endcaps, as depicted in (c). The Co/Fe ring created $\Delta B_0 = -0.9$ T, which is improved to $\Delta B_0 = 0.4$ T in the other configuration. (b) Analysis trap with Co/Fe ring electrode (grey) and other electrodes made from copper. (c) Co/Fe correction electrodes and endcaps (grey) and copper ring and transport electrodes.

B_0. Thus, this approach compensates part of the adverse effect of the increased geometrical factor Λ and B_2 on the cyclotron noise $\sigma_+ \propto B_2 \Lambda / B_0$. In our experiment, where both laser-cooling and a large background field B_0 suppress the cyclotron noise, this effect is negligible. With laser-cooling we operate well inside the energy range where the fidelity is maximized even with ferromagnetic ring electrode.

Clearly, the new approach proposed here would have a more significant effect in experiments with smaller background field B_0 and resistive cooling [33] rather than laser-cooling. This is demonstrated in Fig. 3.6. Here, the spin-flip detection fidelity of a proton in the trap of radius 1.8 mm described in [25] is plotted (blue solid line) compared to a proton in the same trap but with ferromagnetic correction electrodes and endcaps (yellow solid line). The calculation assumes $B_0 = 1.9$ T as in the proton experiment in [1]. Making the correction electrodes and endcaps of this trap from Co/Fe leaves the magnetic bottle invariant while increasing the magnetic field by 1.1 T compared to the ferromagnetic ring. Using the new design, a measurement with resistive cooling at $E_+/k_B = 0.1$ K, as in [1], reaches 98 % detection fidelity
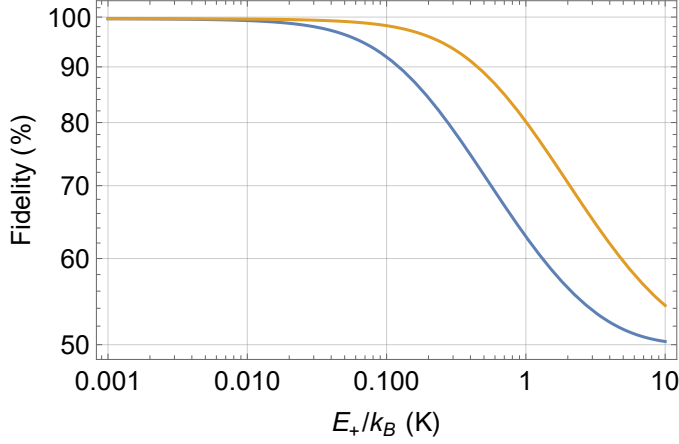
Figure 3.6: Spin-flip detection fidelity of a proton in the analysis trap described in [25] with ferromagnetic ring electrode (blue) compared to a proton in the same trap but with ferromagnetic correction electrodes and endcaps (yellow). Here, white noise of $\sigma_0 = 30$ mHz at averaging time $\tau = 150$ s is assumed. The background field is $B_0 = 1.9$ T as in the proton experiment in [1].

instead of 92 %.

3.3 Optimizing the Magnetic Field

In order to find the relevant parameters that maximize B_0 and B_2, the magnetic field of the simplified correction electrodes shown in Fig. 3.7 is simulated in COMSOL Multiphysics $^\circledR$ [34]. The program calculates the magnetic field numerically on the mesh displayed in Fig. 3.7. The maximum mesh size is reduced to 1 µm along the z-axis in the range

$$-0.5 \text{ mm} \leq z \leq 0.5 \text{ mm},$$

i.e. a range 5 times larger than the approximate axial amplitude of the particle

$$\sqrt{\langle z^2 \rangle} = \sqrt{\frac{k_B T_z}{m \omega_z^2}} \approx 0.1 \text{ mm}$$

at temperature $T_z = 10$ K in order to have a sufficient number of data points for the fit.

The length L, width W and opening angle Θ, as denoted in Fig. 3.7, are varied and B_2 and B_0 determined from a polynomial fit of order 14 of the simulated magnetic field. The results in Fig. 3.8 show that a larger opening angle improves B_0 while $|B_2|$ is maximized at $\Theta = 20$ °. The effect of the width W is negligible compared to that of the length L. As L needs to be at least 4 mm to optimize B_2, or even larger to further increase B_0, not only the correction electrodes but also the endcaps need to be made of Co/Fe with a combined length of approximately 4 mm at $a = 1.25$ mm.
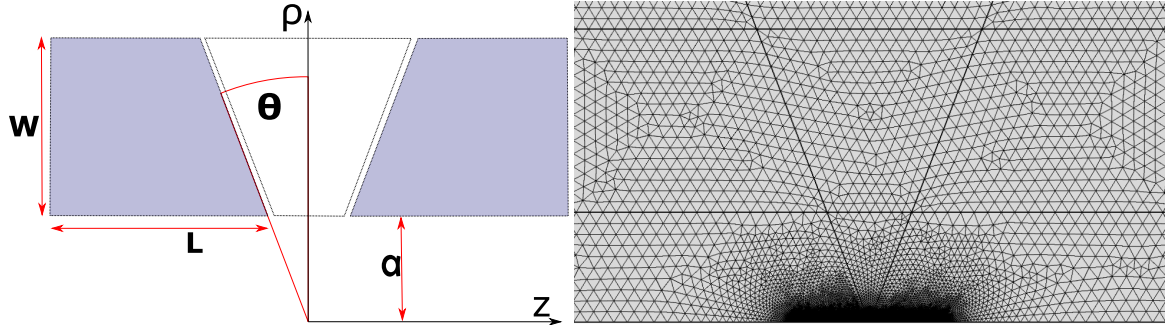
19

Figure 3.7: Simplified correction electrodes made of ferromagnetic material (blue) simulated in COMSOL. *left*: Parameters that are varied in order to optimize the magnetic field. *right*: Mesh used by COMSOL for numerical calculations
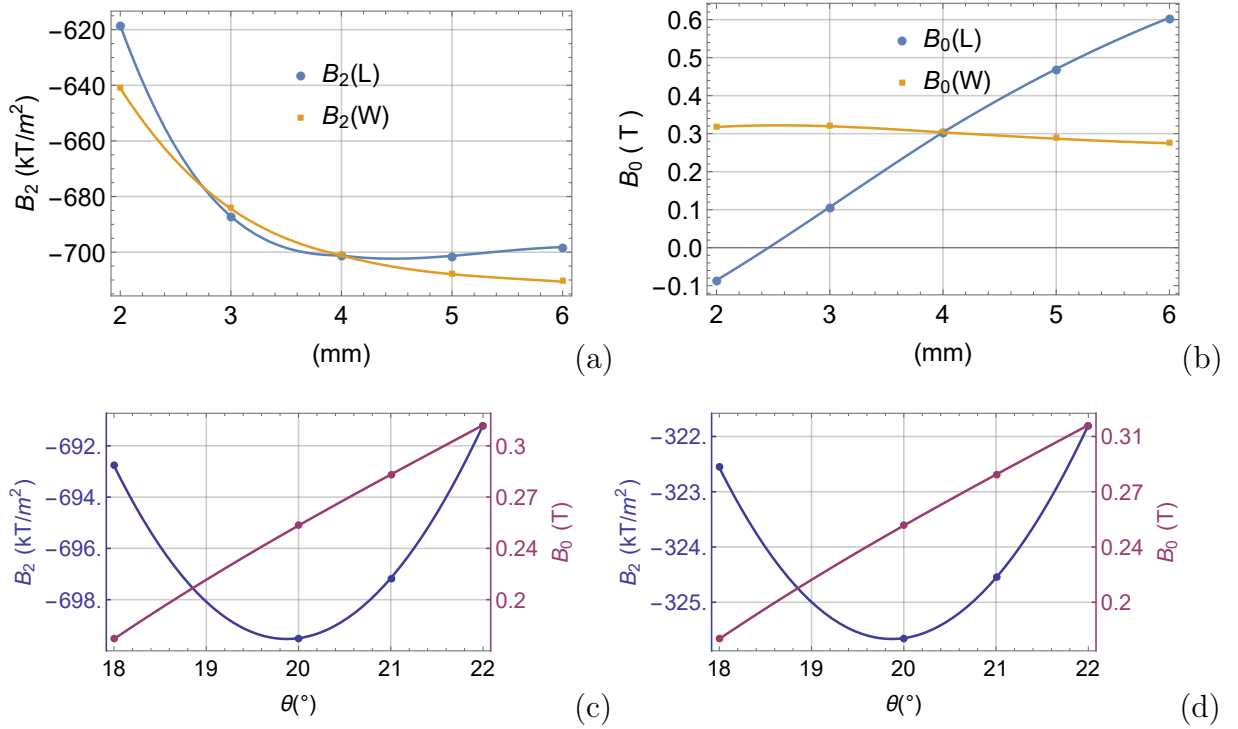
Figure 3.8: (a): B_2 created by the electrode shape in Fig. 3.7 simulated for different lengths L at width $W = 4$ mm as well as different widths W at set length $L = 4$ mm. Here the radius and opening angle remain constant at $a = 1.25$ mm and $\Theta = 21°$. (b): B_0 for the same parameters as in (a). (c): B_2 and B_0 simulated for different opening angles Θ. Here the length, width and radius are fixed at $L = 5$ mm, $W = 4$ mm and $a = 1.8$ mm. (d): Simulation in (c) repeated with smaller radius $a = 1.25$ mm and also accordingly smaller length $L = 4$ mm and $W = 4$ mm.

In Fig. 3.8 (c) an (d), the opening angle Θ is varied at radius 1.25 mm and 1.8 mm, showing that the optimal angle is the same in both cases. This angle implemented in the final geometry, giving $B_2 = -646$ kT m^{-2}, smaller than $B_2 = -699$ kT m^{-2} of the simplified geometry because of the constraints on the ring length due to the electrostatic potential.

3.4 Optimizing the Electrostatic Potential

The electrode lengths used for the magnetic field simulations (Fig. 3.3) are adjusted to achieve a compensated and orthogonal electrostatic potential. The first step, explained in subsection 3.4.1, is to approximate the optimal lengths with an analytical calculation based on a simplified electrode shape. These results are then used as starting points for simulations of the potential of the actual electrode geometry which are described in subsection 3.4.2.

3.4.1 Cylindrical Approximation

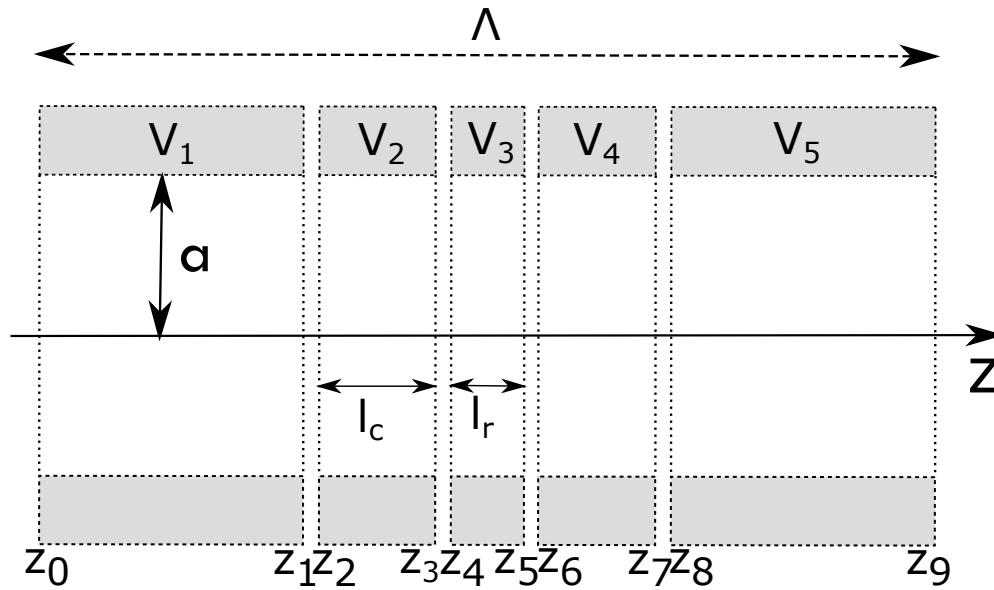Figure 3.9: Simplified, cylindrical geometry of the electrodes with the parameters used for the calculation of the electrostatic potential in Eq. (3.2).

For a first estimate of the adequate electrode lengths and tuning ratio for different radii, a simplified cylindrical geometry as shown in Fig. 3.9 is assumed. With this simplification the expansion coefficients in Eq. (2.7) can be expressed analytically

by

$$C_j = \sum_{n=1}^{\infty} \left[\frac{V_1 \cos(k_n z_0) - V_5 \cos(k_n \Lambda)}{k_n} + \sum_{i=2}^{5} \frac{V_i - V_{i-1}}{k_n^2 d} (\sin(k_n z_{2i}) - \sin(kn z_{2i-1})) \right]$$
$$\cdot \left(\frac{n\pi}{\Lambda} \right)^j \frac{1}{I_0(k_n a)} \sin\left(\frac{n+j}{2} \pi \right) \frac{1}{j! \Lambda V_0},$$

(3.2)

where I_0 is the modified Bessel-function of order zero and $k_n = \frac{n\pi}{\Lambda}$ [35]. Here, the endcap voltages $V_1 = V_5 = 0$ vanish and the voltages applied to the correction electrodes $V_2 = V_4 = V_c$ are equal. $V_3 = V_0$ is the ring voltage. The distance between neighboring electrodes is $d = 0.14$ mm. The lengths of the endcaps $l_e = z_1 - z_0 = z_9 - z_8$ have a negligible effect on the result and are set to 10 cm.

Using this expression the system of equations

$$C_2(l_r, l_c, TR) = 0$$
$$C_4(l_r, l_c, TR) = 0$$
$$d_2(l_r, l_c, TR) = 0$$

is solved using Mathematica.

Fig. 3.10 shows the results for the optimal electrode lengths and tuning ratio as well as the axial frequency that follows from the resulting coefficient C_2 via Eq. (2.2) assuming $V_0 = -0.8$ V. These parameters are used as starting point for finding the optimal parameters in the actual, not cylindrical geometry by simulating the potential as described in the next section.

3.4.2 Simulation

As explained in section 3.3, the electrode shapes are not cylindrical but instead adapted to optimize the magnetic field. The resulting electrostatic potential is then simulated using COMSOL in order to adjust the parameters l_r and l_c.

The ring potential U_r and correction potential U_c at voltage 1 V are simulated separately so that the total potential for any ring voltage V_0 and tuning ratio TR can be calculated via

$$V(z) = V_0(U_r(z) + TR \cdot U_c(z)).$$

(3.3)

Defining r_n and d_n as the multipole expansion parameters of the ring and correction potentials

$$U_r(z) = \sum_n r_n z^n \text{ and } U_c(z) = \sum_n d_n z^n$$

(3.4)

leads to

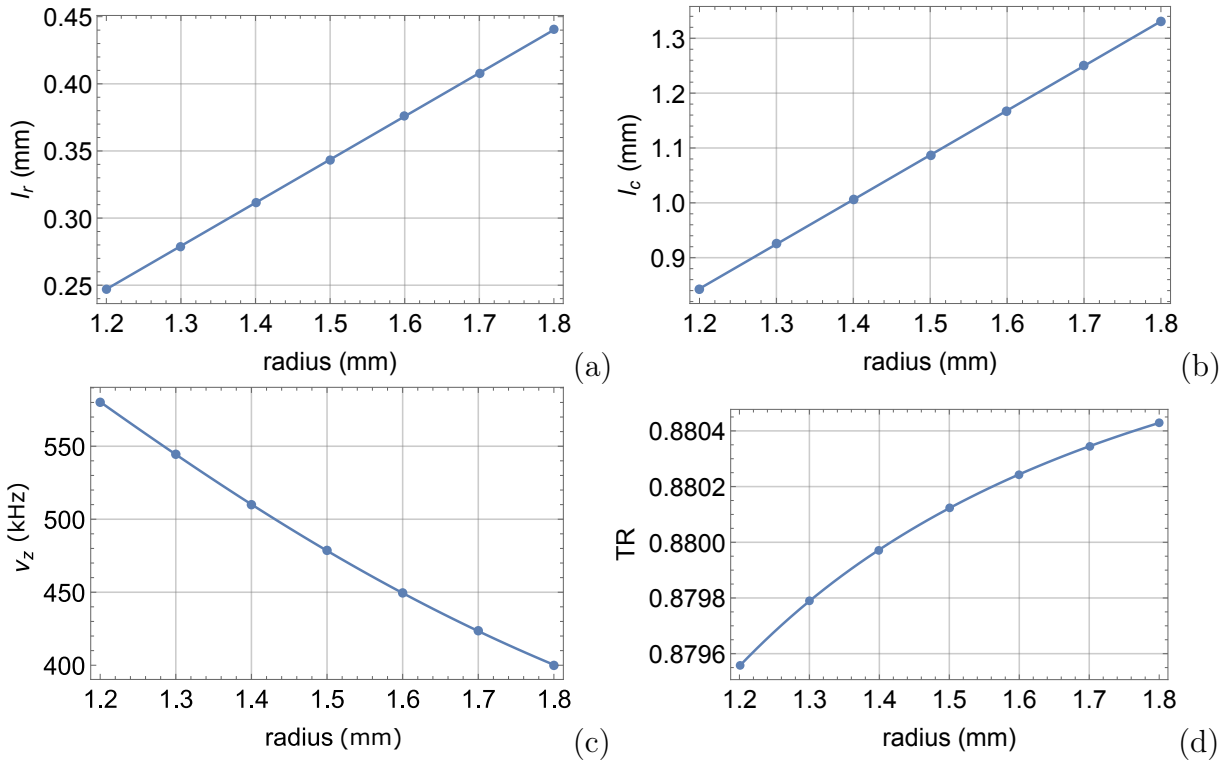$$C_n = r_n + TR \cdot d_n$$

(3.5)

Figure 3.10: (a) Ring length l_r, (b) correction electrode length l_c, (c) axial frequency ν_z for ring voltage $V_0 = -0.8$ V and (d) tuning ratio TR for different radii assuming cylindrical electrodes.
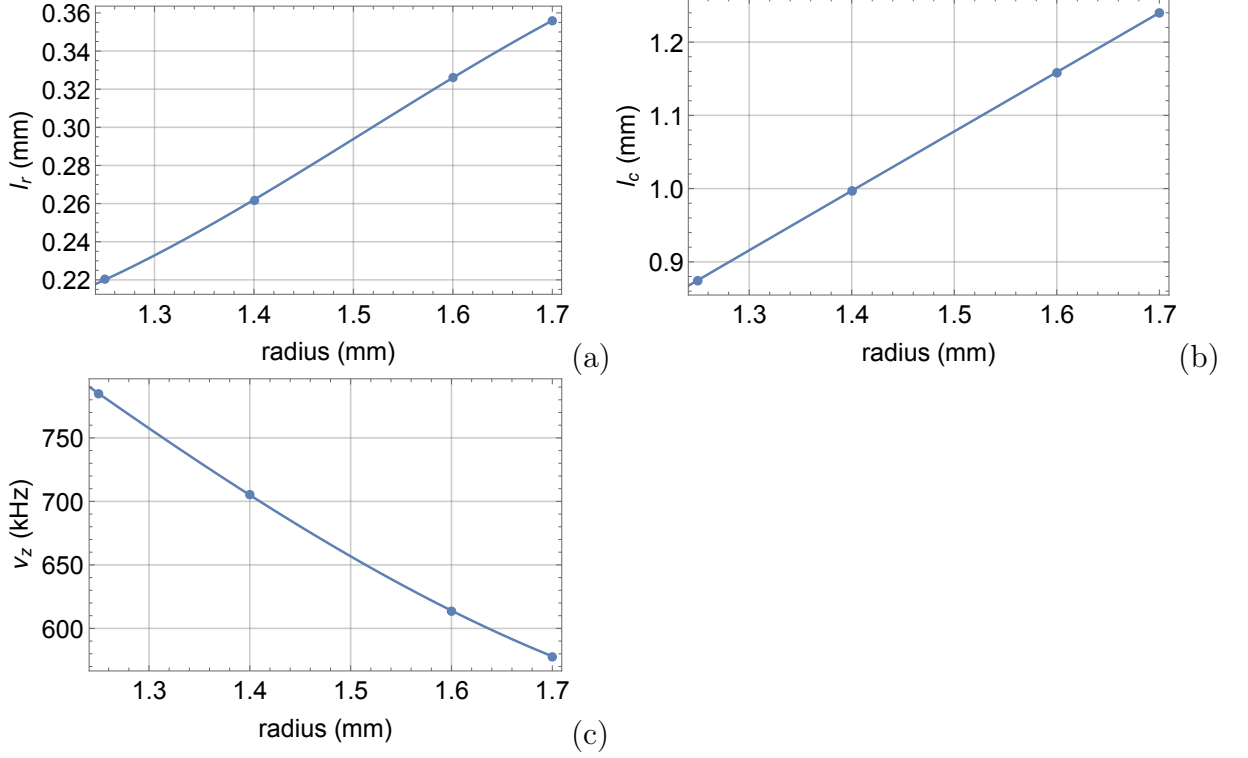
Figure 3.11: (a) and (b): ring length l_r and correction electrode length l_c adjusted for the geometry in Fig. 3.4 with different trap radii to optimize the electrostatic potential as described in section 3.4.2. (c) axial frequency ν_z at ring voltage $V_0 = -0.8$ V.

for the coefficients C_n of the total potential, compare Eq. (2.7)

It follows from Eq. (3.5) that two tuning ratios TR_4 and TR_6 can be found where C_4 and C_6 are zero, respectively. In the optimal geometry the difference $\Delta TR = TR_4 - TR_6$ vanishes, i.e. the trap is compensated.

For a given ring length, ΔTR is determined for two correction electrode lengths close to the one calculated in the last section for cylindrical geometry. The length l_c where $\Delta TR = 0$ is then determined from a linear fit and the simulation is repeated with this value. Afterward the linear fit of $\Delta TR(l_c)$ is repeated including the new data point so as to iteratively improve l_c toward $\Delta TR = 0$. This process ends when l_c is optimized to the order of 1 µm, as the electrodes can not be produced with higher precision.

By this process, the compensated geometry can be found for any assumed ring length. This is repeated for several ring lengths to find D_2 as function of the ring length and determine the optimal value for l_r from a linear fit to $D_2(l_r)$. This way $|D_2|$ can be minimized to the order of $10^2 \frac{\text{Hz}}{TR}$ due to the limit in length precision.

The results in Fig. 3.11 show a significantly smaller l_r than in the cylindrical approximation.

The optimization process described above requires to calculate D_2 and ΔTR for
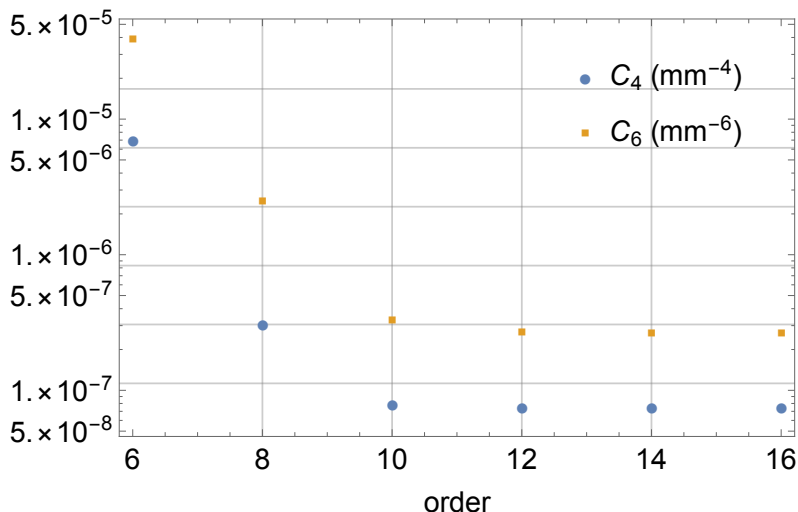
Figure 3.12: C_4 and C_6 in dependence of the order of the polynomial fitted to the total potential assuming 5 digits precision on the tuning ratio $TR = TR_4$.

several geometries. These parameters can most easily be determined by fitting U_r and U_c separately, which gives the parameters C_i via Eq. (3.5). However, this results in uncertainties on ΔTR of the order 10^{-3}. This uncertainty decreases to 10^{-7} by fitting the total potential $U_r + TR \cdot U_c$ for each tuning ratio between $0.86 \leq TR \leq 0.9$ in steps of 10^{-3}. For these fits a polynomial of order 16 and the fit range -0.3 mm $\leq z \leq 0.3$ mm is used. As seen from Fig. 3.12, C_4 and C_6 converged with higher order of the fitted polynomial, being approximately constant from order 12 onward. From these fits follow C_2, C_4, C_6 and thereby also ν_z as functions of the tuning ratio. Linear fits to $C_4(TR), C_6(TR)$ then give TR_4, TR_6 and D_2 is the slope of the fit to $\nu_z(TR)$ for a ring voltage of $V_0 = -0.8$ V.

3.5 Final Trap Parameters

The parameters describing the finalized trap are listed in Tab. 3.1. The theoretical optimal tuning ratio TR_4 is given with 10 digits precision, but is rounded to 5 digits for the calculation of C_4 and C_6 in Tab. 3.1 to estimate a realistic remaining unharmonicity. Assuming that instead six digits accuracy of the tuning ratio is achieved reduces $\Delta\nu_{z,4}/\nu_z$ by one order of magnitude while $\Delta\nu_{z,6}/\nu_z$ remains invariant.

In the precision trap which is positioned 6 cm away from the analysis trap, the magnetic field inhomogeneity caused by the ferromagnetic material of the analysis trap amounts to $\Delta B_{0,PT} = 9$ µT, $B_{1,PT} = -0.4$ mT m^{-1} and $B_{2,PT} = 0.23$ T m^{-2}, which is smaller than in the proton trap [36].

Next to the analysis trap are the transport electrodes leading to the precision trap with radius 3.5 mm. To make the potentials of neighboring electrodes sufficiently overlap for ion transportation, the length-to-radius ratio can not be too large. For

Table 3.1: Parameters of the new analysis trap. For the frequency ν_z and shifts $\Delta\nu_z$, $\Delta\nu_{z,4}$, $\Delta\nu_{z,6}$ a ring voltage of $V_0 = -0.8$ V, charge $q = 2e$, magnetic moment $\mu_I = -1.07 \cdot 10^{-26}$ J T^{-1} and axial temperature 15 K are used.

B_2	ΔB_0	ν_z	$\Delta\nu_{z,\text{SF}}$
-646.4 kT m^{-2}	0.38 T	788.3 kHz	89 mHz
TR_4	TR_6	D_2	C_2
0.8790056437(7)	0.8789300(1)	353 Hz/Unit	-238369 m^{-2}
C_4/C_2^2	C_6/C_2^3	$\Delta\nu_{z,4}/\nu_z$	$\Delta\nu_{z,6}/\nu_z$
$-1.6 \cdot 10^{-5}$	$-8.5 \cdot 10^{-4}$	$-1 \cdot 10^{-8}$	$-5 \cdot 10^{-10}$
$\partial C_4/\partial TR$	$\partial C_6/\partial TR$	l_r	l_c
-0.213 mm^{-4}/Unit	0.144 mm^{-6}/Unit	0.229 mm	0.886 mm

this reason the width of the sapphire rings separating the electrodes in the analysis trap is reduced to 1.3 mm compared to 1.7 mm in the other traps of the setup.

3.6 Seven-electrode Trap with different Ring Radius

As seen in the last chapter, the small trap radius required to maximize B_2 also increases the axial frequency, which has an adverse affect on the spin-flip frequency shift $\Delta\nu_{SF} \propto \frac{B_2}{\nu_z}$. While a smaller ring voltage decreases the axial frequency, the electrode voltages should remain significantly larger than patch potentials which is why $-V_0 \geq 0.8$ V is assumed here. Instead one could design a trap which has $D_2 > 0$ to reduce the axial frequency, however abandoning the orthogonality condition makes it harder to find the optimal tuning ratio where C_4 and C_6 both vanish. A better solution is therefore to increase the radius of the copper ring electrode, minimizing the axial frequency, while leaving the ferromagnetic electrodes at a small radius, maximizing B_2. In a 5-polar trap a harmonic potential can not be achieved in this configuration, so that a seven-electrode trap as in Fig. 3.13 is designed here.

3.6.1 Conditions to the Potential

Analogously to Eq. (3.5) and Eq. (2.6), the expansion coefficients C_n of the total trap potential are

$$C_n = r_n + TR_1 \cdot d_n^{(1)} + TR_2 \cdot d_n^{(2)}, \tag{3.6}$$

so that

$$D_2^i := \frac{\partial\nu_z}{\partial TR_i} = \frac{\nu_z}{2C_2}d_2^i. \tag{3.7}$$

Figure 3.13: Seven-electrode trap geometry with larger ring radius

Here, r_n, $d_n^{(1)}$ and $d_n^{(2)}$ are the multipole expansion parameters of the ring and the two correction potentials.

Again, the trap potential should compensated, that is $C_4 = 0$, $C_6 = 0$, can however not be orthogonal for each correction electrode, as the parameters $d_2^{(1)}$ and $d_2^{(2)}$ never vanish simultaneously. Instead, a modified orthogonality condition

$$D_2^{tot} = 0 \tag{3.8}$$

is posed, defining

$$D_2^{tot} := D_2^{(1)} + \frac{TR_2}{TR_1} D_2^{(2)}. \tag{3.9}$$

Thus, at constant ratio of tuning ratios $\frac{TR_2}{TR_1}$ the trap can be operated similar to an orthogonal five-electrode trap. Also, this modified orthogonality condition implies $C_2 = r_2$, which is small due to the large inner radius of the ring electrode. Operating the trap can also be simplified by setting d_4 of one of the correction electrodes zero so that the condition $C_4 = 0$ only depends on one of the two tuning ratios. As this is only possible for the inner correction electrodes under the given condition, the trap is adjusted to also fulfill

$$d_4^{(1)} = 0. \tag{3.10}$$

Another option would be to leave all electrodes at the same radius, reduce the axial frequency with $d_2^{(2)} > 0$ and fulfill the orthogonality condition with the other correction electrode $d_2^{(1)} = 0$. However, at least when demanding the optimal opening angle $\Theta = 20\,^\circ$ of the ferromagnetic material, $d_4^{(2)} = 0$ can not be simultaneously fulfilled.

3.6.2 Potential Simulation

For the geometry pictured in Fig. 3.13 the potentials U_0, U_{c1} and U_{c2} of the ring and the two correction electrodes are simulated in COMSOL separately, for different electrode lengths while $R_2 = 1.25$ mm remains fixed. This simulation is automatized in a java script for ring lengths 0.4 mm $\leq l_r \leq 1.3$ mm in steps of 0.3 mm, correction lengths l_{c1} and l_{c2} in the range 0.3 mm $\leq l_{c1/2} \leq 2.2$ mm in steps of 0.1 mm and ring radii 2.3 mm $\leq R_2 \leq 2.7$ mm in 0.1 mm steps. The total potential $V_0(U_r + TR_1 U_{c1} + TR_2 U_{c2})$ is fitted with a tenth order polynomial in the z range -0.3 mm $\leq z \leq 0.3$ mm for tuning ratios $0.8 \leq TR_{1/2} \leq 1.2$. For each combination of electrode lengths the tuning ratios TR_1 and TR_2 are found for which C_4 and C_6 vanish. With these parameters also ν_z, $d_{2,4,6}^{(1)}$, $d_{2,4,6}^{(2)}$, C_8 and $D_2^{(1,2)}$ are calculated. The results are interpolated as function of the four lengths R_2, $l_{1,2}$ and l_r and solved for Eqs. (3.8) and (3.10), respectively.

Compared to the five-electrode trap, the parameters TR_2 and l_{c2} and R_r constitute three additional degrees of freedom. Demanding $D_2^{tot} = 0$ and $d_4^{(1)} = 0$ therefore still leaves two remaining free parameters. In order to satisfy Eqs. (3.8) and (3.10), the ring radius is confined to 2.3 mm $\leq R_2 \leq 2.7$ mm. Due to the fixed opening angle $\Theta = 20\,^\circ$ the ring length is limited to the range $l_r < 2(R_2 \tan(\Theta) - 0.14$ mm$)$. In this range neither $C_8 = 0$, nor $d_6^{(1)} = 0$ can be achieved additionally to fix the free length parameters. In Fig. 3.14 the axial frequency of ^{3}He^{2+} and the resulting spin-flip frequency shift $\Delta\nu_{z,SF}$ are plotted as function of the ring radius and length. While the effect of the ring length is negligible, choosing the largest ring radius slightly improves the spin-flip frequency shift. In Tab. 3.2 the trap parameters are given for the case $l_r = 1.1$ mm and $R_2 = 2.7$ mm.

Both $D_2^{(1)}$ and $D_2^{(2)}$ are $2 \cdot 10^6$ Hz/Unit for all possible l_r and R_r so that a sufficient frequency stability requires a voltage supply with 7 channels operating around 1 V in order to achieve a constant tuning ratio. In this case the ratio of signal-to-frequency noise caused by voltage instability

$$\frac{\Delta\nu_{z,SF}}{\frac{\partial\nu_z}{\partial V_0}\frac{\Delta U}{U}} = \frac{\Delta\nu_{z,SF}}{\frac{\Delta U}{2U}\nu_z} \propto \frac{1}{\nu_z^2} \tag{3.11}$$

lies in the range 40 to 70 compared to 8 for the five polar trap introduced in the last section. Otherwise, as a worst case estimate where the three voltages fluctuate independently with $\frac{\Delta U}{U}$ the resulting signal-to-noise ratio is

$$\frac{\Delta\nu_{z,SF}}{\frac{\Delta U}{U}\sqrt{(\nu_z/2)^2 + (TR_1 D_2^{(1)})^2 + (TR_2 D_2^{(2)})^2}} \approx 3. \tag{3.12}$$
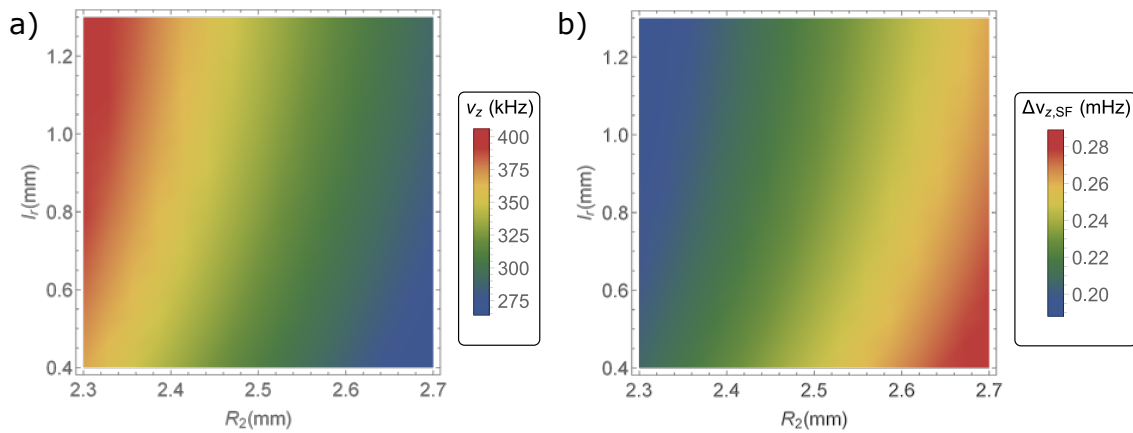
Figure 3.14: (a) Axial frequency and (b) spin-flip frequency shift assuming $V_0 > V_{c1} > V_{c2} = 1$ V.

Table 3.2: Parameters of the seven-electrode analysis trap when choosing the ring length $l_r = 1$ mm and $R_2 = 2.7$ mm. For the nuclear spin-flip frequency shift, the voltages $V_0 > V_{c1} > V_{c2} = 1$ V are assumed. The relative frequency shift due to C_8 is calculated for an axial temperature of 10 K.

l_r	l_{c1}	l_{c2}	R_2
1 mm	0.389 mm	1.949 mm	2.7 mm
B_2	ΔB_0	ν_z	$\Delta\nu_{z,\mathrm{SF}}$
-700 kT m^{-2}	0.4 T	285788 Hz	267 mHz
TR_1	TR_2	D_2^{tot}	$\Delta\nu_{z,8}/\nu_z$
0.84727210(1)	0.81654239(1)	$2.7 \cdot 10^{-11}$ Hz/Unit	$-5 \cdot 10^{-9}$
$D_2^{(1)}$	$D_2^{(2)}$	$d_4^{(1)}$	$d_4^{(2)}$
$2.17 \cdot 10^6$ Hz/Unit	$-2.26 \cdot 10^6$ Hz/Unit	$-2 \cdot 10^{-18}$ mm^{-4}	-0.016 mm^{-4}

4 ^{3}He source

Producing the ^{3}He$^+$ and ^{3}He^{2+} ions for the experiment requires releasing helium atoms inside the trap which can then be ionized, in our case via electron impact using an electron gun with field emission point. As an external gas inlet would compromise the vacuum, an internal source is much preferable but poses a special difficulty for noble gases such as helium. Despite its very low reactivity a sufficient amount of helium has to be bound and retained in vacuum to only be released when heated. The required amount of helium is roughly estimated in the following.
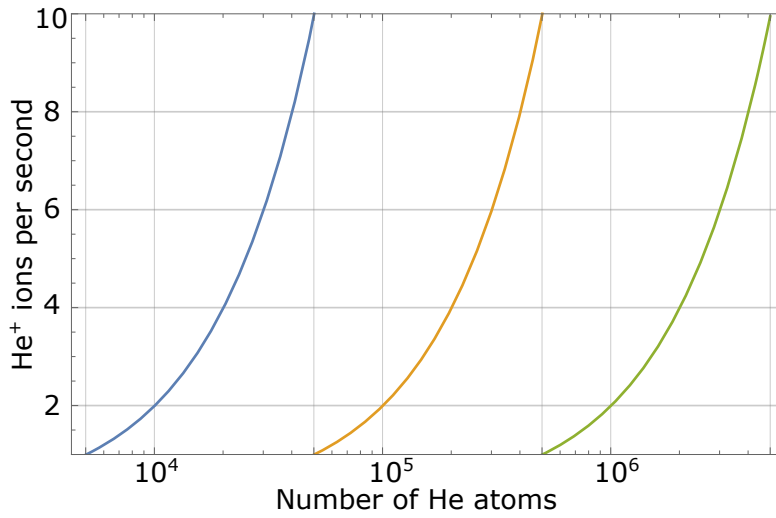

Figure 4.1: Production rate of ^{3}He$^+$ ions as function of the number of helium atoms in case of an electron current of 1 nA (green), 10 nA (yellow) and 100 nA (blue). For details see text.

The cross sections for single and double ionisation of helium by electron impact are $\sigma_1 = 4 \cdot 10^{-21}$ m^2 and $\sigma_2 = 1 \cdot 10^{-23}$ m^2 [37, 38] at their maxima at 100 eV and 250 eV, respectively. At a realistic electron current of $I = 10$ nA the rate of ionization in a cloud of N_{He} helium atoms spread in a trap of radius $r = 2$ mm and volume V is

$$R = N_{\mathrm{He}}\sigma v_e \frac{N_e}{V} = \frac{N_{\mathrm{He}}\sigma}{\pi r^2}I/e. \tag{4.1}$$

For the rate to be of the order of $1/s$ the number of helium atoms has to be $N_{\mathrm{He}} \approx 10^5$, which should be released in a short time span as the trap stack is cryogenically pumped continuously.
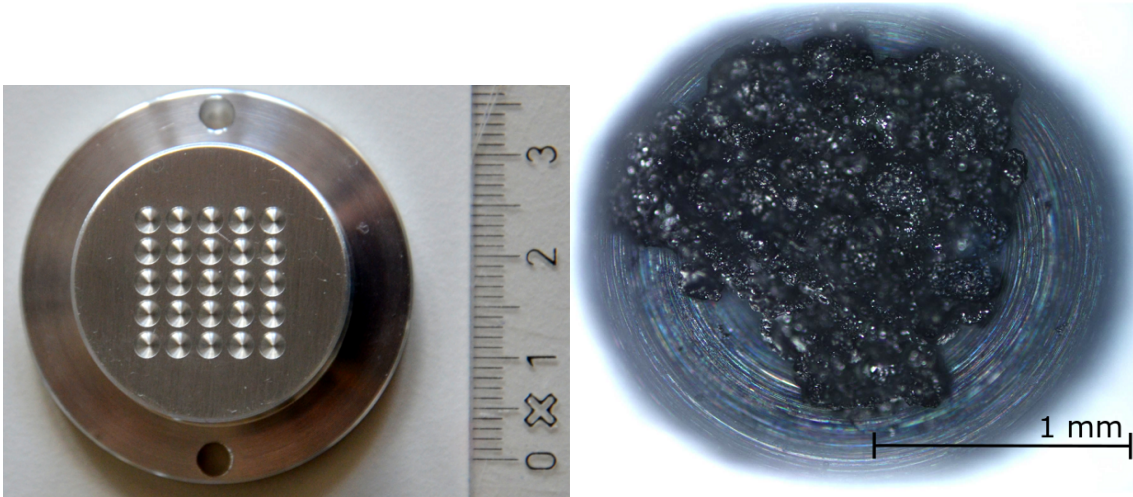
Figure 4.2: *Left:* Aluminium sample holder with holes for 25 samples. *Right:* Titanium sponge sample C1.

Due to the trap potential, the $^3\text{He}^+$ ions will accumulate in a much smaller volume than the ^3He atoms. With a magnetron radius of $r_- \approx 10$ µm, a single $^3\text{He}^+$ ion will be doubly ionized in the order of 100 s. Thus, a helium source that releases 10^5 atoms per seconds is sufficient to create both charge states.

4.1 Titanium filament

Titanium is a possible carrier for ^3He since it can retain macroscopic amounts of helium in its crystalline structure when helium-3 is produced after beta decay of tritium in titanium hydride (TiH_2) [39]. Because of the long half-life of tritium and also to avoid having to handle a radioactive ^3He-source, we test whether helium can be directly loaded into a titanium filament by heating the filament in helium atmosphere.

4.1.1 Sample preparation/ loading

The materials tested are titanium foil (thickness 2 mm, purity 99.2 %) and titanium sponge (diameter $\leq$ 3 mm, purity 99.9 %), both from AlfaAesar [40, 41]. They were cleaned with isopropanol and afterwards baked out in an oven at 600 °C in vacuum (10^{-6} mbar). The oven containing the samples is preheated up to 600 °C for approximately 3.5 h, left at 600 °C for 10 min and then turned off and immediately flooded with helium-4 from a gas bottle so that the pressure in the oven was at least 1 mbar. The pressure could not be determined precisely because of the steep characteristic curve of the Pirani pressure gauge in a helium atmosphere [42]. The samples then remained exposed to the helium while the oven cooled down.

This procedure was repeated with a second batch of samples two months later

in order to check for a decline of the helium concentration in the titanium with time. In the second attempt the titanium had turned dark blue when taken out of the oven, most likely because of a reaction with hydrogen and oxygen due to an imperfect vacuum. Unlike in the first loading attempt, the maximum temperature was 650 °C and the samples had remained in the oven after switching off for about 20 min before the helium was added.

In order to make sure that the vacuum apparatus described in the next section where the helium concentration in the titanium is measured does not get flooded with too much helium, the samples were not to weigh more than ~ 8 mg. Therefore, grains of diameter ≤ 1 mm were picked from the titanium sponge and equally small foil pieces. For a third and fourth batch of samples the masses were determined up to 0.1 mg, see Tab. 4.1. The samples were loaded into the aluminum holder shown in Fig. 4.2 which was first cleaned in an ultrasonic cleaner.

Table 4.1: Loading and measurement dates, storage temperatures and masses of titanium samples of which the helium content is determined. Compare Figs. B.1 and B.3 in the appendix.

sample	type	^{4}He loaded	measured	temp.	mass (mg)	oxidized
A1	foil	not loaded	July 11, 2018	300K	-	no
A3	foil	April 24, 2018	July 11, 2018	300K	-	no
A4	foil	June 20, 2018	July 11, 2018	300K	-	yes
C1, E1	sponge	not loaded	July 11, 2018	300K	-	no
C3, E3	sponge	April 24, 2018	July 11, 2018	300K	-	no
C4, E4	sponge	June 20, 2018	July 11, 2018	300K	-	yes
F3	sponge	not loaded	Dec 17, 2018	300K	5.6(1)	no
F4	sponge	not loaded	Dec 17, 2018	300K	9.8(1)	no
F5	sponge	not loaded	Dec 17, 2018	300K	4.4(1)	no
H5	sponge	Oct 9, 2018	Dec 17, 2018	300K	4.1(1)	yes
I5	sponge	Oct 9, 2018	Dec 17, 2018	300K	4.5(1)	yes
J5	sponge	Oct 9, 2018	Dec 17, 2018	300K	3.3(1)	yes
H3	sponge	Oct 9, 2018	Dec 17, 2018	70K	2.8(1)	no
I3	sponge	Oct 9, 2018	Dec 17, 2018	70K	3.1(1)	no
J3	sponge	Oct 9, 2018	Dec 17, 2018	70K	3.0(1)	no
H4	sponge	Dec 5, 2018	Dec 17, 2018	300K	3.3(1)	no
I4	sponge	Dec 5, 2018	Dec 17, 2018	300K	3.8(1)	no
J4	sponge	Dec 5, 2018	Dec 17, 2018	300K	6.1(1)	no

4.1.2 Setup

The titanium samples were analyzed in the noble gas laboratory of Prof. Henner Busemann at ETH Zuerich in the setup sketched in Fig. 4.3, which is designed to

measure the noble gas content of meteorite samples.

The measurement apparatus consists of an UHV system (10^{-10} mbar), which is attached to a static sector-field mass spectrometer, where a static magnetic field diverts the different isotopes according to their charge-to-mass ratio after ionization through electron bombardment at 45 eV. The ions can then be detected either by a Faraday collector or a secondary electron multiplier (SEM) if higher sensitivity is required.

The gas extraction system consists of an 1064 nm Nd:YAG laser connected to a camera and a screen. Below the laser is a window to the sample port which can be adjusted in position with three screws to bring one of the samples into focus to melt it.

For purification, the extracted gas is directed through three pipes that reach into liquid nitrogen filled bottles, so-called cold traps, as well as two getters. The getters are reactive metal alloys kept at 350 °C which remove reactive gas molecules like hydrogen, methane, various other hydrocarbons, ammonia, water, carbon monoxide and carbon dioxide. In the cold traps contaminations like argon and water are frozen, thereby also reducing the interference of doubly charged ^{40}Ar on ^{20}Ne. One of the cold traps is filled with activated charcoal in order to increase its surface. Here, the heavy noble gases argon, krypton and xenon are frozen onto the charcoal, while the lighter noble gases helium and neon have lower freezing temperatures.

The cold traps are cleaned once a day by replacing the liquid nitrogen with 80 °C hot water to unfreeze the contaminations. The charcoal trap gets additionally heated to 200 °C with a heater to release trapped argon.

For calibration measurements, bottles containing a mixture of noble gases with known pressure and composition can also be connected to the system by a valve.

4.1.3 Measurement

First, the sample port is preheated in UHV at 120 °C for one day to reduce atmospheric gas contamination. It follows a blank measurement, where the laser is aimed at the aluminum holder instead of a sample to detect background gas that gets released from the walls, where residual gases from previous measurements are adsorbed, or from neighboring samples that partly degas when the aluminum holder heats up. Afterwards the helium content of the nine titanium samples is determined in the following steps.

1. **gas extraction**
   The sample port is separated from the rest of the system by closing the valves on both sides (L1, L2 in Fig. 4.3). The laser is started manually and stops automatically after one minute. Meanwhile the power is continuously increased starting at 50 % of the maximum power of 25 W and the sample holder is constantly shifted so that the laser is moved across the whole sample in order to melt it. However, if too much material evaporates from the sample and
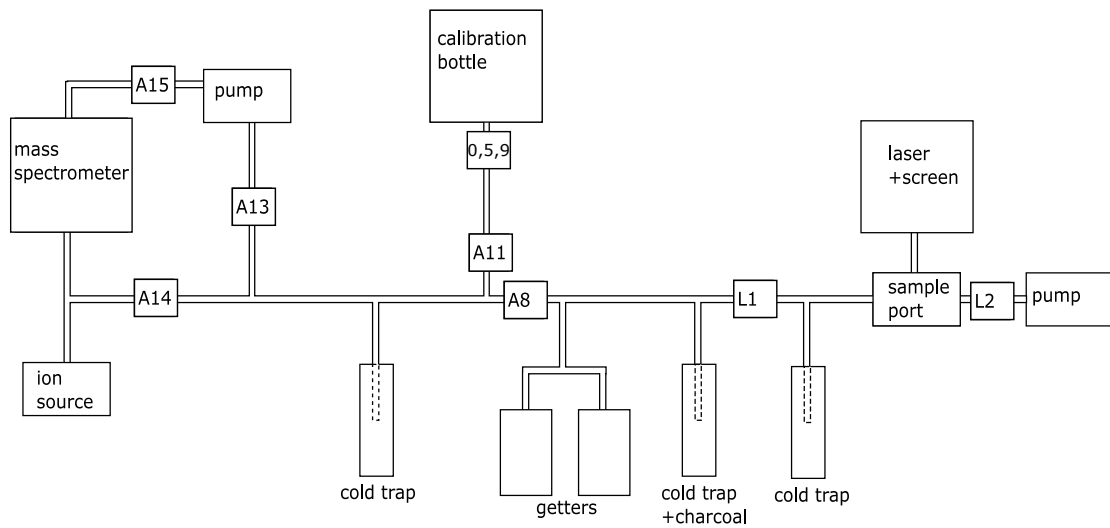
Figure 4.3: Schematic illustration of the most important valves and instruments of the noble gas spectrometer at ETH Zürich. For details see text.

condenses on the port window, it absorbs part of the laser light and the sample does not melt entirely.

2. **gas purification**
Valve L1 is opened and the gas is allowed to expand up to A8 during a 4 min wait. The volume now reaches into the two getters, and the second cold trap for another 10 min.

3. **spectrometry**
, Opening the valves A8 and A14 allows the gas to expand to the mass spectrometer. Also opening valve A11 assures that the gas occupies the same volume as during calibration. Now the background ions (hydrogen, methane, water, fluorine, argon and carbon dioxide) are measured first with both the Faraday cup and the electron multiplier, successively. From this, the right magnetization strength for the mass spectrometer is calibrated. The system is separated by closure of A8 and A11 and valves 0,5,9 are opened to ensure that the gas occupies the same volume as the gas from the standard bottles during calibration. Opening L2 allows the volume to the right of A8 to be pumped off. Now ^{4}He as well as the isotopes ^{3}He, ^{20}Ne, ^{21}Ne, ^{22}Ne are measured. The meteorite pieces that were loaded into the same sample holder as the titanium could degas when the titanium is molten and the holder heats up. This would be recognizable from the relative amounts of the different helium and neon isotopes.

Each mass is measured sequentially in five to eight cycles. Several analysis

cycles are necessary to record the time dependence of the ion current of each isotope and extrapolated to time zero, when the gas was let into the spectrometer. Gas contaminations that adhere to the surfaces in the mass spectrometer can be released during the measurement leading to a constant increase in measured number of atoms.

Finally, the instrument's sensitivity is determined by measuring the content of one of the calibration bottles.

4.1.4 Results

The first step of the data reduction was carried out using a program provided by the ETH, which plots the counts or currents versus time and derives the intercept at time $t = 0$ from a linear fit, see Fig. 4.4. The hot blank, where the laser heated the aluminium holder at 90 % power for one minute, is assumed as background.

The calibration bottle contained too much ^{4}He to be measured using the SEM while the samples contained not enough helium to be detectable with the Faraday cup. Therefore, the same calibration factor as for ^{3}He is assumed for ^{4}He as the instrumental mass discrimination affects the result by only a few percent. The standard amount of ^{3}He in the calibration bottle is $1.6965 \cdot 10^{-8}$ cm^{3}STP. In order to find the amount of gas released from the bottle in the n-th calibration measurement, this value is multiplied by d^n, where $d = 0.999636$ is the so-called dilution factor. The number of helium atoms is calculated from the volume V at STP via $N = p_0 V/(k_B T_0)$, using the standard pressure and temperature $p_0 = 1013$ mbar and $T_0 = 273$ K.

In the first measurement, nine samples (A1-E4) were tested and the remaining 16 slots in the aluminium holder were filled with meteorite samples from ETH Zuerich. These meteorites are rich in helium-3 with a ^{4}He-to-^{3}He ratio of $R_m \approx 5$. It can thus be assumed that all detected ^{3}He atoms N_3 are a contamination from a neighbouring meteorite sample which also got heated. In this case, the number of ^{4}He atoms released from the meteorites in a measurement of a titanium sample is $N_m = R_m N_3$. With this correction and after subtracting the hot blank, none of the foil samples but all sponge samples contained measurable amounts of ^{4}He. As seen from Fig. B.2, the samples C3 and C4 have similar mass, suggesting that 90 % of the helium diffused out of the titanium sponge in two months at room temperature.

It was therefore tested in a second measurement whether the helium is contained longer if the sponge is stored at low temperature. To this purpose, the samples H3, I3, and J3 remained at normal pressure in a CF16 chamber surrounded by liquid nitrogen over this period of time. The results in Tab. 4.3 show that both at room temperature and at cryogenic temperatures, the ^{4}He concentration dropped by 99 % in eight weeks. To avoid a helium leak in the vacuum chamber, a different loading method is required, where the helium is not only adsorbed at the surface. One option is to use ^{3}He rich meteorites as mentioned above, where the helium atoms are implanted deeply into the structure by cosmic rays [43].
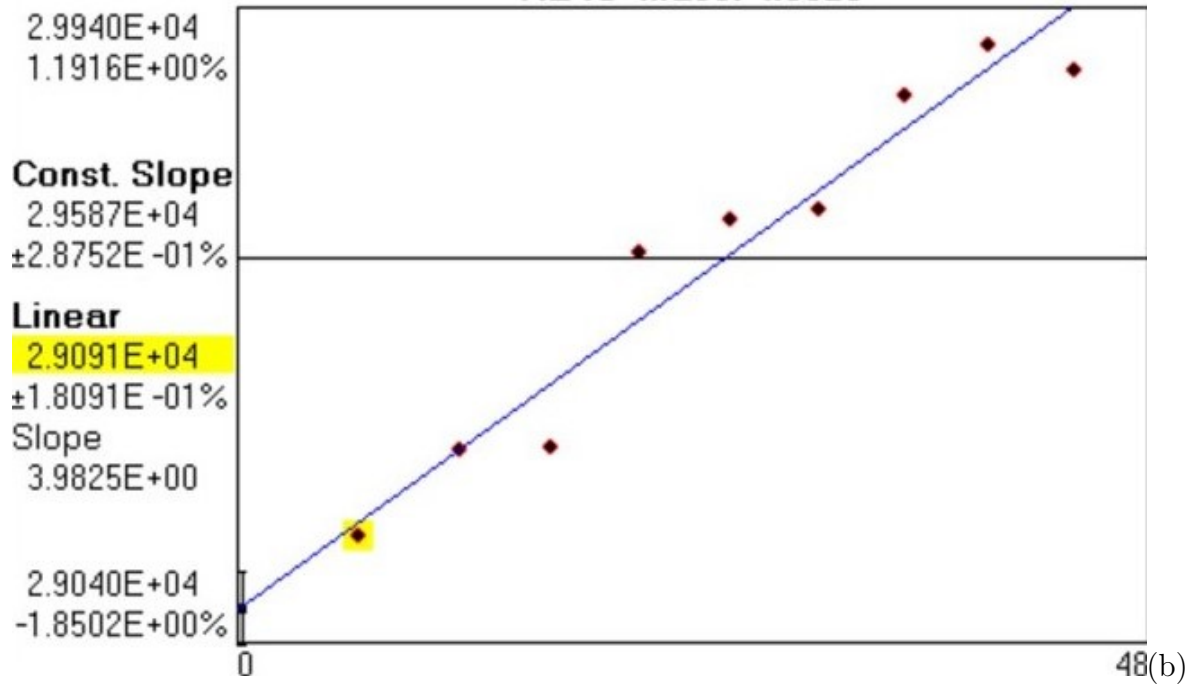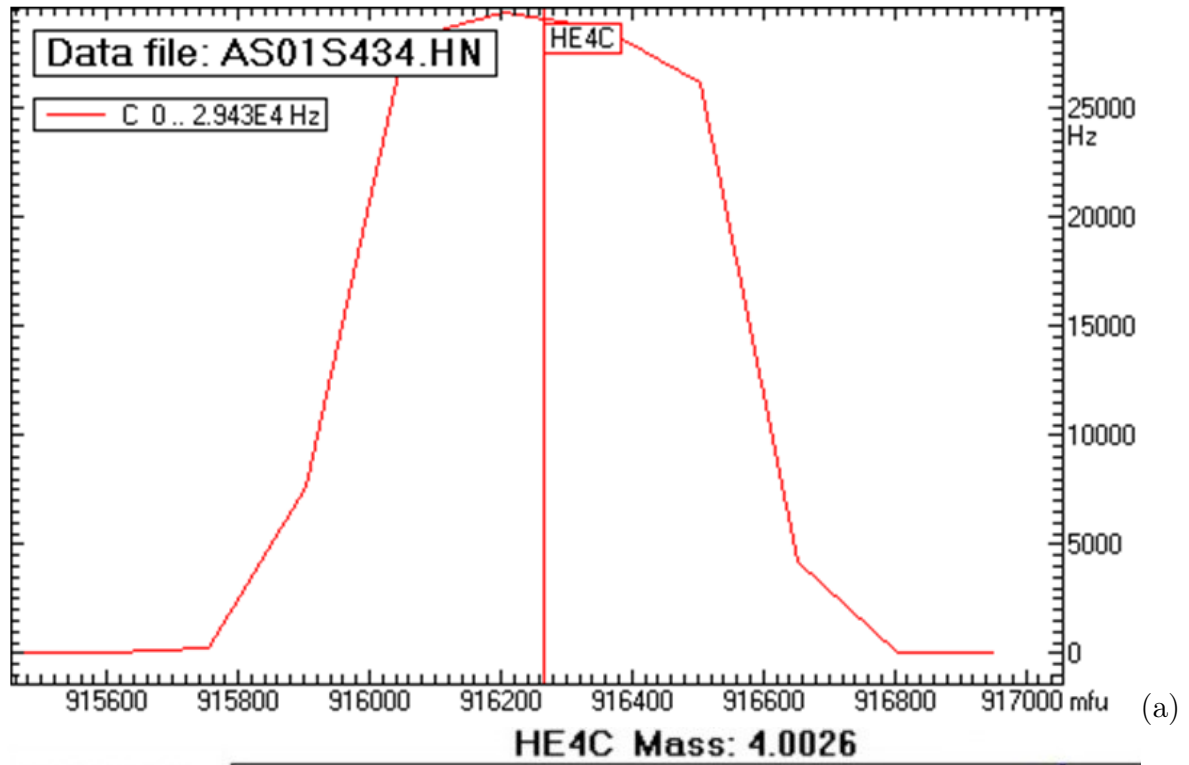
(a)

(b)

Figure 4.4: (a) ^{4}He rate as function of the magnetic field for sample E4 measured with the SEM. (b) ^{4}He rate measurements of sample E4 vs. time in minutes. The linear fit gives the rate at time zero and the uncertainty in Tab. 4.2.

Table 4.2: Measured ³He and ⁴He rates, ³He-to-⁴He ratio and the number of ⁴He atoms after subtracting the contribution from the meteorites N_m, see above. The number of atoms in the last column is calculated from the rate using the calibration measurement.

sample	⁴He rate (Hz)	³He rate (Hz)	³He/⁴He (%)	⁴He atoms (10^9)
hot blank	1023(5)	2(1)	0.2(1)	1.86(2)
A1	886(8)	86(1)	9.7(2)	0.84(1)
A3	655(34)	34(4)	5.3(7)	0.89(5)
A3	4775(19)	750(7)	15.7(2)	1.88(1)
C1	442(12)	19(1)	4.4(3)	0.63(2)
C3	12701(54)	9(2)	0.07(2)	23.3(1)
C4	97432(320)	14(1)	0.015(1)	179.1(7)
E1	2140(10)	258(3)	12.1(2)	31.56(1)
E3	1955(18)	1(1)	0.07(4)	3.58(3)
E4	29091(53)	2(2)	0.006(7)	53.5(1)

4.2 Glass Sphere

Another option for an internal ³He source is a glass sphere containing ³He which is heated in order to regulate the strongly temperature dependent permeation rate. In this manner He atoms can be extracted when required for loading the trap, while at 4K the rate of released atoms is negligible. Except for rubber, glass and in particular fused silica is the material most easily permeated by helium [44].

4.2.1 Permeation Estimates

Permeation of a gas through a solid wall proceeds in the following steps:

- impact of the atoms on the surface

- adsorption

- solution in the solid

- diffusion due to the concentration gradient

- desorption on the low pressure side.

The concentration $\phi = Sp$ of gas atoms in the glass is proportional to the partial pressure p via the solubility S. A pressure difference Δp between both sides of the wall of thickness d therefore corresponds to a concentration gradient $d\phi/dx = S\Delta p/d$. According to Fick's first law the diffusion flux, i.e. the number of atoms flowing through a unit area during a unit time interval, is $\vec{J} = -D\nabla\phi$, where D is

Table 4.3: Measured ^{4}He rates and corresponding helium concentration in the titanium samples

sample	^{4}He rate (Hz)	^{4}He atoms per mg Ti (10^9/ mg)
hot blank	30(5)	-
F3	44(3)	0.005(2)
F5	1233(10)	0.6(1)
H3	15415(28)	11.4(4)
I3	9797(31)	6.5(2)
J3	23540(49)	16.3(5)
H5	7109(17)	7.8(1)
I5	17102(61)	3.6(1)
J5	6264(17)	3.9(1)
H4	$3142(9) \cdot 10^3$	1971(60)
I4	$3311(20) \cdot 10^3$	1804(49)
J4	$4302(18) \cdot 10^3$	1460(25)

called the diffusion coefficient. Thus, the number of atoms flowing through the wall of thickness d and area A is

$$\dot{N} = -ADS\Delta p/d. \tag{4.2}$$

The diffusion coefficient in solids at temperature T is well predicted by the Arrhenius equation $D = D_0 \exp \frac{-Q}{RT}$, where R is the universal gas constant and Q the material dependent activation energy. Compared to the diffusion coefficient, the temperature dependence of the solubility is negligible [45].

Defining the permeability $K(T) = DS = K_0 \exp \frac{-Q}{RT}$, the permeation rate then is

$$\dot{N} = K(T)A/d\Delta p = K(T)A/d\frac{Nk_BT}{V}. \tag{4.3}$$

Here, Δp is the pressure difference between the in- and the outside of the glass sphere. It is equal to the pressure inside the glass sphere which is placed in the vacuum chamber at around 10^{-15} mbar. The resulting differential equation (4.3) is solved by $N(t) = N(t=0)\exp(t/\tau(T))$ with time constant $\tau = Vd/(KAk_BT)$. As the time constant τ is of the order of days up to 500 K and one year at room temperature, the permeation rate is well approximated using the initial number of helium atoms $N(t=0)$. This leads to

$$\dot{N} = KA/dp_0T/T_0 \tag{4.4}$$

for a glass sphere which was filled at temperature T_0 with helium pressure p_0. In the experiment the initial pressure is $p_0 = 5$ mbar at temperature $T_0 = 293$ K. In case of quartz, measurements [44] show $Q/R = 2458$ K and $K_0 = 3.94 \cdot 10^{-7}$ cm^{3}at

NTP s^{-1} cm^{-2} mm. The resulting permeation rate is plotted in Fig. 4.5 as function of the temperature for the sphere radius $r = 5$ mm and wall thickness $d = 1$ mm. At 4 K the rate is negligible, while at around 140 K the required 10^5 helium atoms per s are reached.
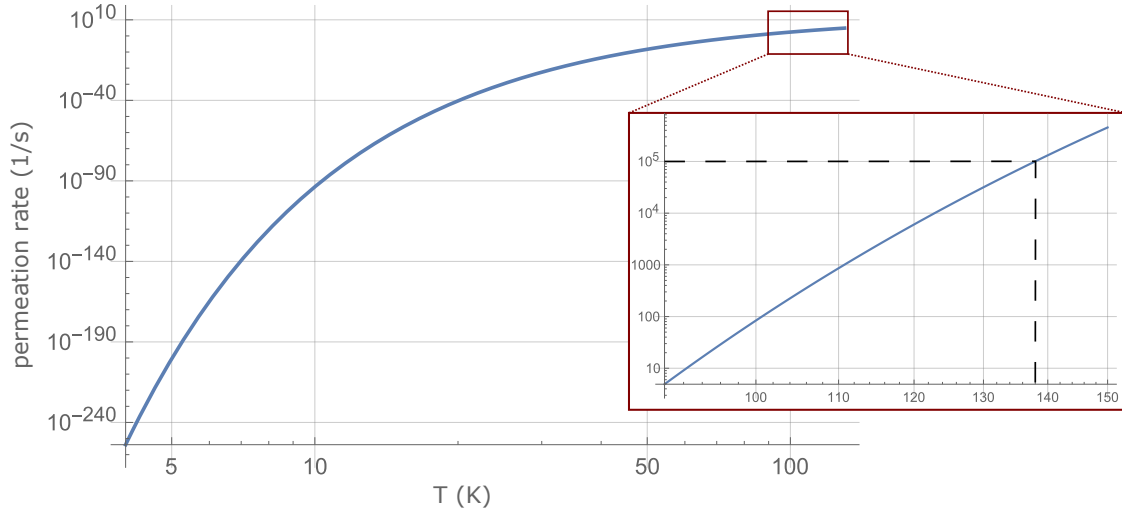

Figure 4.5: Number of helium atoms which diffuse out of the quartz sphere per second as function of the temperature.

Heating Methods

The necessary heating power can be reduced by separating the glas sphere from the trap electrodes with a distance holder made of teflon, which has a low thermal conductivity of $\lambda_T = 0.25$ W m^{-1} K^{-1}. Specifically, with a $l = 4.5$ mm long teflon ring with outer and inner diameter $r_o = 10$ mm and $r_i = 9$ mm, as used in the setup described in the next section, a temperature difference of $\Delta T = 140$ K between the electrode at approximately 4 K and the sphere can be achieved with $P = \lambda_T \Delta T \Pi (r_o^2 - r_i^2)/l = 0.3$ W. This power can most easily be reached with heating resistors. Alternatively, a high-powered laser can be utilized, however only a small percentage of the laser power will be absorbed by the glass. With an ablation laser with 200 mJ per pulse at a maximal rate of 30 Hz the power calculated above can not be reached at around 1 % absorption at the wavelength of a Nd:YAG laser. Instead, this technique is suitable to locally heat the glas at the laser focus for a short time, only releasing the helium atoms solved in the glas at this spot rather than the atoms inside the sphere. This could be sufficient to extract 10^5 atoms, as according to [45] the solubility of helium in quartz is approximately $10^{14} \frac{\text{atoms}}{\text{cm}^3 \text{ mbar}}$.
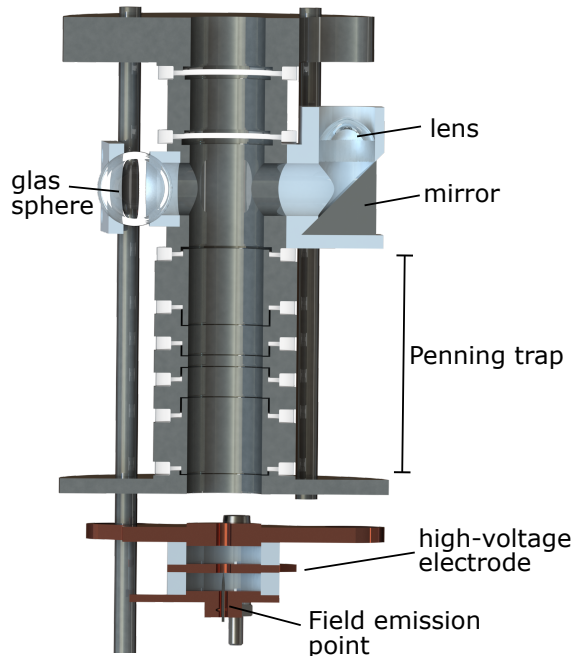
Figure 4.6: Penning trap with target- and dummy electrode on top and the electron gun below. The teflon-conter which retains the glass sphere is screwed to the teflon holder for the lens and right-angled mirror.

4.2.2 Test Setup

In a Penning-trap setup the glass sphere is tested as a ^{3}He source with both heating resistors and an ablation laser. The helium atoms are ionized using a field emission point and detected in the trap with an axial resonator.

Trap and Target

The Penning trap used in the test setup consists of five cylindrical electrodes of inner radius 3.5 mm made of gold-plated copper. Above, the target electrode is placed which has two opposing holes of diameter 7 mm. On one side, a plano-convex lens (EFL 30, BFL 28.01, diameter 7.5, YAG-BBAR coating) and a right angled mirror in a teflon holder focus the laser beam on the front of the quartz sphere on the other side of the target electrode.

The quartz sphere was coated with indium using an ultrasonic soldering iron leaving a hole of diameter 9 mm where the laser enters as well as a small hole on the opposing side behind which a photo diode is placed. The diode helps aiming the laser on the target, while the indium layer serves to minimize reflections which might also hit the diode. For the same purpose the four other sides of the right angled mirror and a copper tube bridging the gap between the CF16 tube and the lens are coated with graphite. Four 50 Ω SMD thinfilm resistors rated for a power of 1 W are mounted around the sphere with thermal conducting glue (*Electrolube*
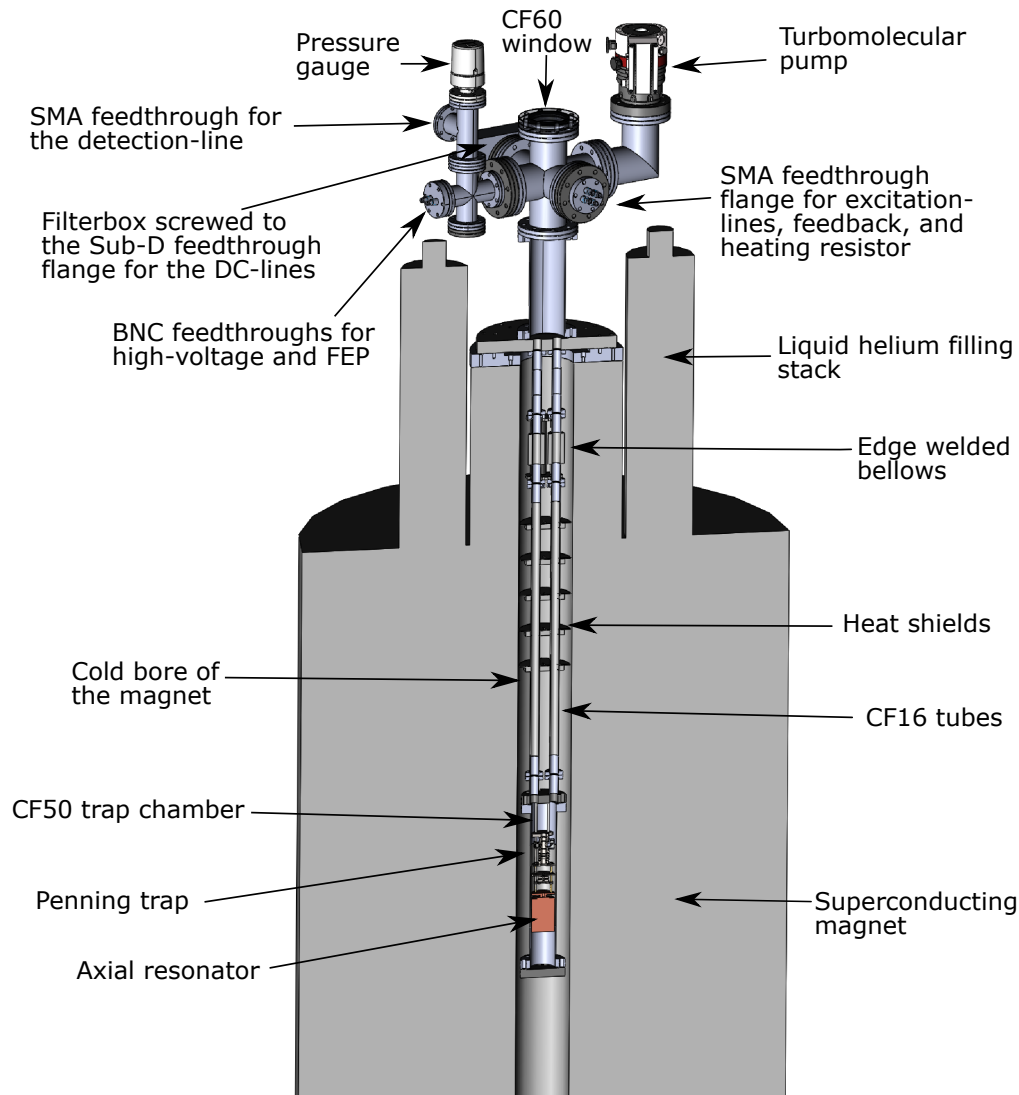
Figure 4.7: Setup placed in the cold bore of the 5 T superconducting magnet.

TBS20S) and connected with copper wire in series. With a 7 Ω connection cable, applying a voltage of 29 V will deliver a thermal output of 1 W per resistor at a current of 140 mA.

Ablation laser

The Nd:YAG ablation laser (*Litron Lasers* Nano S 60-30, 200 mJ max output, $3 - 7$ ns pulse duration) and the alignment laser (*Thorlabs* handheld laser source, 635nm, < 5mW) are placed on the optical table in the laboratory above the magnet room. Both beams are collimated with a combination of a bi-convex and a bi-concave lens, aligned using a semi-transparent mirror and finally directed through the hole in the floor onto the bredboard on top of the setup in the magnet room.

Vacuum apparatus

The trap is located in the vertical cold bore of a superconducting magnet at the center of the magnetic field $B \approx 5$ T. On top of the setup a CF60 double-cross with separate flanges for the DC supply-, excitation- and detection-line feedthroughs as well as the turbopump and a window is placed. Above the window a bredboard is attached where the laser beam is collimated with lenses a second time. The laser is directed through one and the cables through a second CF16 stainless steel tube towards the CF50 chamber where the trap is placed. In order to reduce the heat input and thereby the liquid helium consumption in the magnet, each CF16 tube is connected to an edge welded bellow with $n = 61$ convolutions. The bellows are kept at length $L = 150$ mm by GFK tubes because of their low heat conductivity. Five heat shields, i.e. aluminium plates with diameter 2 mm smaller than the magnet bore, are fixed along the CF16 tubes. The spaces in between the shields are stuffed with cotton so that the vaporized helium is forced to rise slower out of the setup, cooling it on the way, while the helium heats up from 4 K to room temperature.

Wiring

Inside the aluminium box screwed onto the DC-flange, the first filter stage with RC low pass filters for the DC-lines is placed. For the DC-lines manganin wires are used because of their small heat conductance. Starting from room temperature the lines are guided to a second filter board, screwed to the top-plate above the trap (see Fig. 4.7). On this board also the excitation-lines are filtered, using 18 pF/180 pF capacitive voltage dividers as shown in the wiring diagram below (Fig. 4.8). The AC-lines are cryogenic coaxial cables, where the shielding is made from CuNi and the inner conductors are made from brass. Both on top of the sphere and at the axial resonator a cryogenic thermometer (*Lakeshore* Cernox CU-CX-1030/1050) is placed, of which the resistance is measured with the 4 wire technique. One end of the ring of heating resistors is grounded while to the other end a voltage is applied using a cryo-coax because of its smaller resistance of 7 Ω compared to manganin wires with 30 Ω.
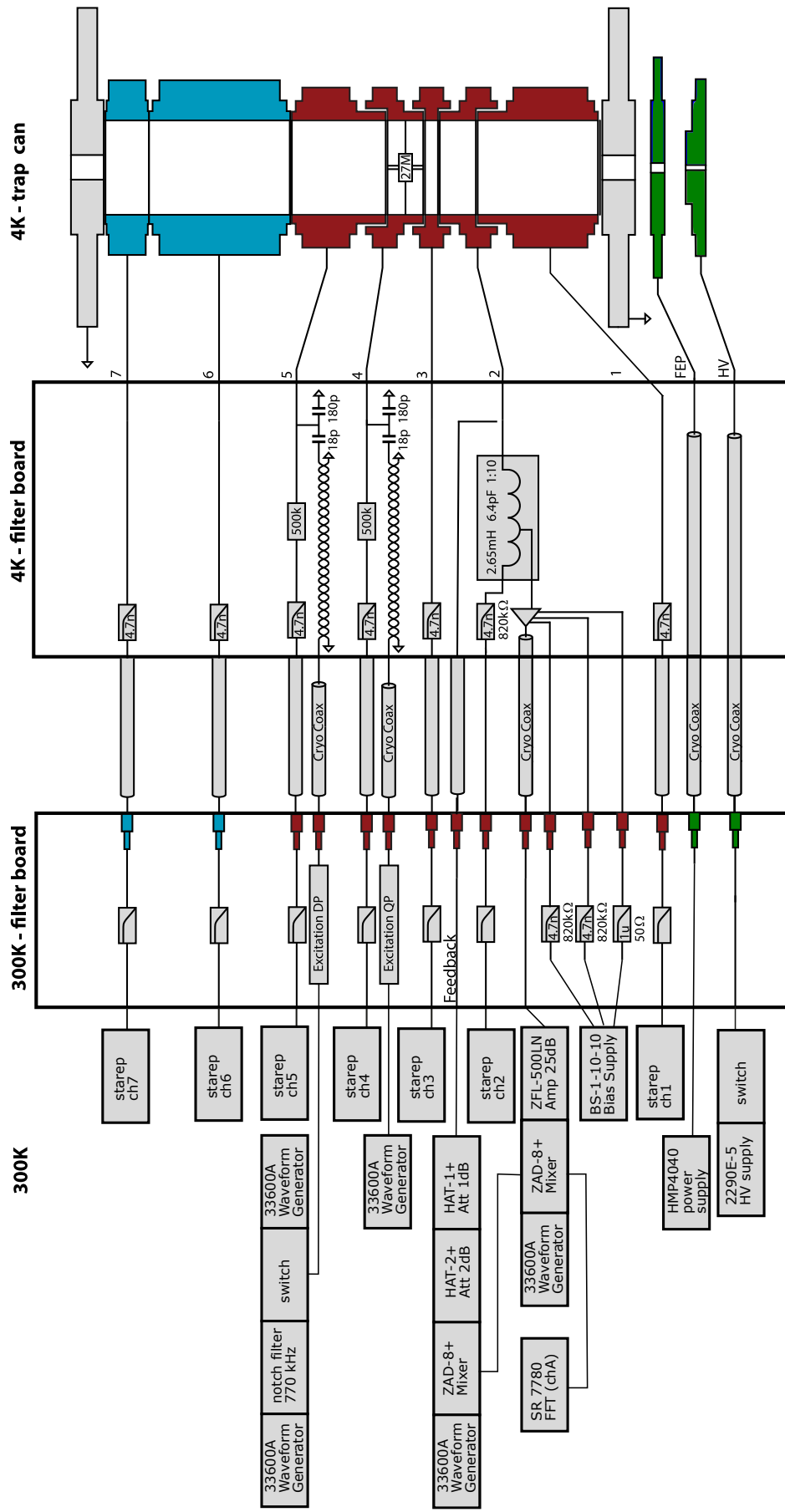
Figure 4.8: Wiring diagram of the setup used to non-destructively detect ^{3}He$^+$ ions in the Penning trap. The ions are created by releasing ^{3}He from the glass sphere and subsequent electron impact ionization.

Detection System

The oscillation of the stored ion induces tiny image currents of the order of fA in the trap electrodes, which can be detected via the voltage drop over an externally connected resonance circuit picked up by a cryogenic amplifier. A coil with inductance L together with the total parallel circuit capacitance C_{total}, consisting of the trap capacitance and parasitic self-capacitances of the coil and the wiring, forms a parallel tuned circuit with resonance frequency $\omega_{\mathrm{LC}} = 1/\sqrt{LC_{total}}$. On its resonance frequency the circuit acts as an effective parallel resistance $R_p = \omega_{\mathrm{LC}}LQ$. Here the quality factor Q is defined by the ratio of the stored electromagnetic energy to the energy loss per cycle

$$Q = \frac{\nu_{\mathrm{LC}}}{\Delta\nu}, \tag{4.5}$$

where $\Delta\nu$ is the -3dB width of the resonance curve. Since the voltage drop is $U = R_p I$, the effective parallel resistance R_p has to be as large as possible. An ion which is sufficiently excited to overcome the thermal noise of the resonator can be detected as a peak at the resonance frequency of the ion. If the ion is at thermal equilibrium with the circuit, a sharp minimum appears at the ion's oscillation frequency, which can be understood as a short cut of the thermal noise of the resonator by the ion. For n ions, the -3dB width of this dip is [35]

$$\nu_z(n) = \frac{n}{2\pi} \frac{R_p}{D_{\mathrm{eff}}^2} \frac{q^2}{m}. \tag{4.6}$$

In the experiment, the resonator for the axial frequency measurement is realized as a superconducting wire wound around a toroidal coil body, which is placed inside a cylindrical copper housing below the FEP. For the wire NbTi is used, a type II superconductor with comparatively high critical field $B_{\mathrm{cr}} \approx 14$ T, while the coil body is made from teflon, a dielectricum with low losses due to dissipative polarization currents. This serves to achieve a low energy loss per oscillation cycle, i.e. a large Q-factor. A copper braided hose is screwed to the bottom of the copper housing on one end and the lower flange of the trap chamber on the other end in order to guarantee sufficient thermal coupling to reach the critical temperature $T_{\mathrm{cr}} \approx 10$ K of NbTi.

For a test measurement, the resonator was connected to one of the correction electrodes of the trap (compare Fig. 4.8) and cooled to 4 K with a pulse tube cooler. Measuring the resonance curve with a network analyzer gives the resonance frequency $\nu_{\mathrm{LC}} = 745.9$ kHz and from the -3dB width $\Delta\nu$ the Q-value $Q = 60000$.

Field Emission Point (FEP)

The electron gun consists of three stacked electrodes, i.e. the base electrode to which the FEP is fixed, the HV-electrode and a grounded shield electrode. They are separated by MACOR rings, see Fig. 4.7. When a high voltage is applied to the

middle electrode, electrons tunnel out of the FEP due to the large electric field which scales with the inverse of the tip radius. The FEP was fabricated, as described in [46], by electrochemically etching a 0.2 mm thick tungsten wire in a NaOH solution. It was tested by applying a high voltage to the HV-electrode in a vacuum chamber at $9 \cdot 10^{-8}$ mbar and measuring the voltage drop over the 11 MΩ input resistance of a voltmeter connected to the FEP-electrode and ground. The measurement showed 0.2 nA at 200 V and 8 ± 2 nA at 250 V, sufficient to ionize ^{3}He in the setup.

Results

With the setup placed in the superconducting magnet, the axial resonator frequency $\nu_{\mathrm{res}} = 861.1$ kHz and Q-value 3000 are measured using a network signal analyzer after mixing the signal down by $\nu_{\mathrm{LO}} = 800$ kHz, compare Fig. 4.8. In a simulation, the theoretical tuning ratio $TR = 0.8808$, as defined in Eq. (2.5), and $C_2 = -30583$ m^{-2} are found. These parameters are determined more exactly by preparing a proton and ^{4}He$^+$ dip. First, ions are loaded to the trap by biasing the FEP with -30 V and applying 850 V to the HV-electrode, resulting in an electron current of 30 nA. A series LC-circuit with resonance frequency 772.1 kHz is connected to the axial excitation-line at one of the endcaps and serves as a notch filter used to clean the trap. In order to remove other ion species from the trap, the ring voltage is first adjusted to bring either protons or ^{4}He$^+$ in resonance with the notch filter. Noise with amplitude 0.8 Vpp and bandwidth 3 MHz is then applied to the filter for 10 s and finally the ring voltage dropped to $V = -0.8$ V for 1 s, releasing the excited ions. The magnetron mode is cooled by coupling the axial and magnetron mode while the axial mode is resistively cooled [33]. To this purpose, the coupling frequency $\nu_{\mathrm{rf}} \approx \nu_- + \nu_z$ is fed to the quadrupole excitation-line which is connected to a split correction electrode, see Fig. 4.8. By afterwards scanning the ring voltages and tuning ratios around the theoretical value, the proton dip and ^{4}He$^+$ dip (Fig. 4.9 (a) and (b)) are found at ring voltages $V = -5.092$ V and $V = -19.978$ V, respectively, with tuning ratio 0.866.

In order to determine the magnetron frequency, the rf-drive is tuned over the resonance $\nu_{\mathrm{rf}} \approx \nu_- + \nu_z$ so that both sidebands $\nu_{r/l} = \nu_z \pm \Omega$ appear in the spectrum, where Ω is the Rabi frequency. From the measured frequencies ν_l and ν_r of the resulting double dip, see Fig. 4.9 (c) and (d), the magnetron frequency can be calculated via [35]

$$\nu_- = \nu_z + \nu_{\mathrm{rf}} - (\nu_l + \nu_r). \tag{4.7}$$

From the measured ^{4}He$^+$ ring voltage and coupling frequency $\nu_- + \nu_z = 877990$ Hz follow the expected values for ^{3}He$^+$: $V = -14.98$ V and $\nu_- + \nu_z = 873869$ Hz. For loading ^{3}He, the heating resistor is operated at 300 mW for 20 s. In order to maximize the single ionization cross section of helium, the FEP is biased with -100 V at reduced high voltage 200 V to reach the same electron current. Afterwards a temperature of (60 ± 3) K is measured at the glass sphere. In order to enhance the

Q-factor the feedback-line as depicted in Fig. 4.8 is attached. The trap is cleaned and the magnetron mode cooled at $\nu_- + \nu_z = 873828$ Hz as depicted in Fig. 4.9 (e). Additionally the cyclotron mode is cooled with a sweep from 28.1 MHz to 28.4 MHz, around the calculated lower sideband $\nu_+ - \nu_z$. The dip in Fig. 4.9 (f) then appeared at ring voltage $V = -14.89522$ and tuning ratio $TR = 0.8725$. The measured quality factor with feedback $Q = 6000$ corresponds to an line width of 2.2 Hz per $^3\text{He}^+$ ion, where the effective electrode distance $D_{\text{eff}} = 7.38$ mm [47] and inductance $L = 1.5$ mH are inserted. Thus the measured $^3\text{He}^+$ dip corresponds to approximately 5 ions. Due to the high FEP biasing, the electron energy is lager than the minimum of 67 eV required for the production of $^{12}\text{C}^{4+}$, so that the dip can not conclusively be identified as $^3\text{He}^+$. The measurement should therefore be repeated with lower FEP bias or with doubly ionized ^3He. At FEP bias -30 V, $^3\text{He}^+$ could already be observed during magnetron cooling, see Fig. 4.9 (e). As a next step, the necessary heating power to produce a single $^3\text{He}^+$ ion should be determined so as to minimize the number of helium atoms released into the closed trap chamber of the setup for the magnetic moment measurement.
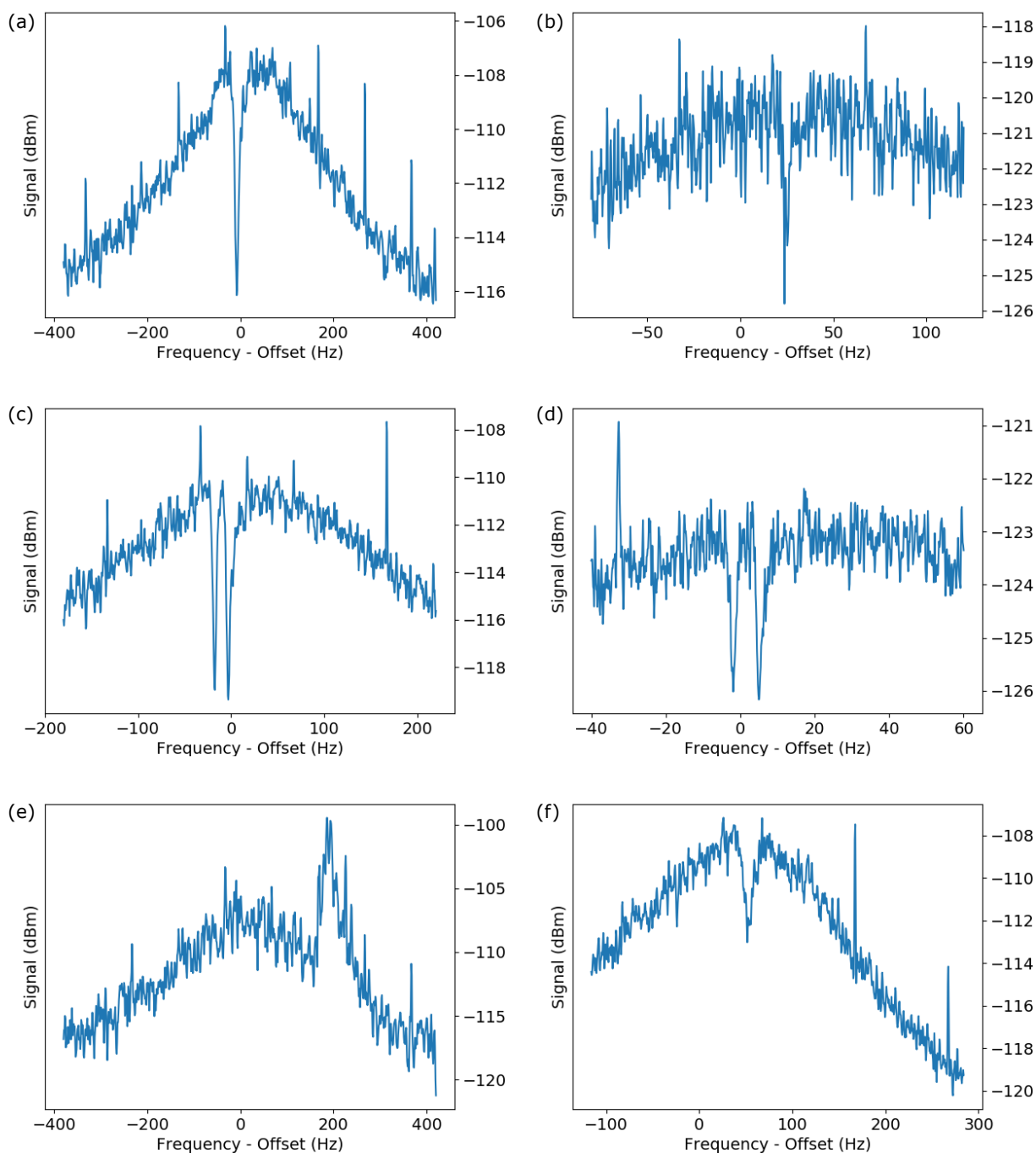
Figure 4.9: (a) and (b): Dip in the noise spectrum of the axial resonator measured with (a) protons and (b) $^4\mathrm{He}^+$. (c) and (d): Magnetron double dip of (c) protons and (d) $^4\mathrm{He}^+$. (e) Magnetron cooling of $^3\mathrm{He}^+$. (f) $^3\mathrm{He}^+$ or $^{12}\mathrm{C}^{4+}$ dip. The offset of the axial frequency axis is the resonator frequency 861.1 kHz. In (f), feedback is applied, causing the shift of the axial frequency of approximately 50 Hz.

5 Conclusion

The major challenge in the magnetic moment determination of $^3\text{He}^{2+}$ compared to the proton is the decreased signal-to-noise ratio in the detection of spin-flips. Therefore, a new analysis trap optimized for nuclear spin-flip detection was designed in this thesis, using analytical and FEM calculations. Due to its small radius, the analysis trap creates a large magnetic bottle B_2, thereby reaching a spin-flip frequency shift in the axial oscillation frequency of 89 mHz for $^3\text{He}^{2+}$ at trapping potential -0.8 V, compared to 60 mHz with the proton trap in [31]. This allows for a nuclear spin-flip detection with a fidelity of 86 % at a realistic white noise level of $\sigma_0 = 35$ mHz. Additionally, a seven-electrode analysis trap was developed that reduces the axial frequency at a given ring voltage and thus further increases the nuclear spin-flip frequency shift to 276 mHz. Also, a new approach with ferromagnetic correction electrodes and endcaps instead of a ferromagnetic ring was introduced. This minimizes the magnetic field at the trap center and as a consequence suppresses the noise caused by cyclotron quantum jumps.

In the second part of the thesis an internal ^3He-source was developed so as to avoid an external inlet which would compromise the 10^{-15} mbar vacuum of the Penning trap. To this end, titanium samples were loaded by heating them to 600 °C and then exposing them to a helium atmosphere. Subsequently the helium concentration in the titanium was measured with a noble gas spectrometer. It could be shown that the samples were loaded with a sufficient amount of helium by this technique but loose 90 % of their helium content within two months. The same results were found with cryogenically stored samples, indicating that such a filament would leak helium into the trap chamber. Therefore, another design was tested, a ^3He-filled quartz sphere which due to the strongly temperature dependent permeation coefficient of glass, releases helium only when heated. To this purpose, a Penning trap setup with detection system was built, where $^3\text{He}^+$ ions were detected after heating the glass sphere at 300 mW for 20 s using a heating resistor. In upcoming measurements, the number of ions at different heating powers and duration can be determined in order to find the minimal required heating and also verify that no helium is released at zero heating power. In the long term, the new Penning trap setup based on the design in this thesis will be installed and eventually the magnetic moment of $^3\text{He}^{2+}$ measured.

A Bibliography

[1] G. Schneider, A. Mooser, M. Bohman, N. Schön, J. Harrington, T. Higuchi, H. Nagahama, S. Sellner, C. Smorra, K. Blaum, Y. Matsuda, W. Quint, J. Walz, and S. Ulmer, "Double-trap measurement of the proton magnetic moment at 0.3 parts per billion precision," *Science*, vol. 358, no. 6366, p. 1081, 2017.

[2] C. Smorra, S. Sellner, M. J. Borchert, J. A. Harrington, T. Higuchi, H. Nagahama, T. Tanaka, A. Mooser, G. Schneider, M. Bohman, K. Blaum, Y. Matsuda, C. Ospelkaus, W. Quint, J. Walz, Y. Yamazaki, and S. Ulmer, "A parts-per-billion measurement of the antiproton magnetic moment," *Nature*, vol. 550, p. 371, 2017.

[3] Y. I. Neronov and A. E. Barzakh *Zh. Eksp. Teor. Fiz*, vol. 75, no. 5, p. 1521, 1978.

[4] J. L. Flowers, B. W. Petley, and M. G. Richards, "A measurement of the nuclear magnetic moment of the helium-3 atom in terms of that of the proton," *Metrologia*, vol. 30, no. 2, p. 75, 1993.

[5] Y. I. Neronov and N. N. Seregin, "Precision determination of the difference in shielding by protons in water and hydrogen and an estimate of the absolute shielding by protons in water," *Metrologia*, vol. 51, no. 1, p. 54, 2014.

[6] D. Budger and D. F. J. Kimball, *Optical Magnetometry*. Cambridge University Press, 2013.

[7] A. Nikiel, P. Blümler, W. Heil, M. Hehn, S. Karpuk, A. Maul, E. Otten, L. M. Schreiber, and M. Terekhov, "Ultrasensitive 3he magnetometer for measurements of high magnetic fields," *The European Physical Journal D*, vol. 68, no. 11, p. 330, 2014.

[8] A. Rudzinski, M. Puchalski, and K. Pachucki, "Relativistic, qed, and nuclear mass effects in the magnetic shielding of h3e," *The Journal of Chemical Physics*, vol. 130, no. 24, p. 244102, 2009.

[9] A. Rudzinski, M. Puchalski, and K. Pachucki, "Relativistic, qed, and nuclear mass effects in the magnetic shielding of h3e," *The Journal of Chemical Physics*, vol. 130, no. 24, p. 244102, 2009.

[10] K. Jackowski, M. Jaszunski, and M. Wilczek, "Alternative approach to the standardization of nmr spectra. direct measurement of nuclear magnetic shielding

in molecules," *The Journal of Physical Chemistry A*, vol. 114, no. 7, p. 2471, 2010.

[11] G. W. Bennett, B. Bousquet, H. N. Brown, G. Bunce, R. M. Carey, P. Cushman, G. T. Danby, P. T. Debevec, M. Deile, H. Deng, S. K. Dhawan, V. P. Druzhinin, L. Duong, F. J. M. Farley, G. V. Fedotovich, F. E. Gray, D. Grigoriev, M. Grosse-Perdekamp, A. Grossmann, M. F. Hare, D. W. Hertzog, X. Huang, V. W. Hughes, M. Iwasaki, K. Jungmann, D. Kawall, B. I. Khazin, F. Krienen, I. Kronkvist, A. Lam, R. Larsen, Y. Y. Lee, I. Logashenko, R. McNabb, W. Meng, J. P. Miller, W. M. Morse, D. Nikas, C. J. G. Onderwater, Y. Orlov, C. S. Özben, J. M. Paley, Q. Peng, C. C. Polly, J. Pretz, R. Prigl, G. zu Putlitz, T. Qian, S. I. Redin, O. Rind, B. L. Roberts, N. Ryskulov, Y. K. Semertzidis, P. Shagin, Y. M. Shatunov, E. P. Sichtermann, E. Solodov, M. Sossong, L. R. Sulak, A. Trofimov, P. von Walter, and A. Yamamoto, "Measurement of the negative muon anomalous magnetic moment to 0.7 ppm," *Phys. Rev. Lett.*, vol. 92, no. 16, p. 161802, 2004.

[12] H. Iinuma and J.-P. N. g-2/EDM experiment collaboration, "New approach to the muon g–2 and edm experiment at j–parc," *Journal of Physics: Conference Series*, vol. 295, no. 1, p. 012032, 2011.

[13] M. Abe, Y. Murata, H. Iinuma, T. Ogitsu, N. Saito, K. Sasaki, T. Mibe, and H. Nakayama, "Magnetic design and method of a superconducting magnet for muon g2/edm precise measurements in a cylindrical volume with homogeneous magnetic field," *Nuclear Instruments and Methods in Physics Research Section A: Accelerators, Spectrometers, Detectors and Associated Equipment*, vol. 890, p. 51, 2018.

[14] M. W. Smith, *Developing the Precision Magnetic Field for the E989 Muon g-2 Experiment.* PhD thesis, University of Washington, 2017.

[15] W. Liu, M. G. Boshier, S. Dhawan, O. van Dyck, P. Egan, X. Fei, M. Grosse Perdekamp, V. W. Hughes, M. Janousch, K. Jungmann, D. Kawall, F. G. Mariam, C. Pillai, R. Prigl, G. zu Putlitz, I. Reinhard, W. Schwarz, P. A. Thompson, and K. A. Woodle, "High precision measurements of the ground state hyperfine structure interval of muonium and of the muon magnetic moment," *Phys. Rev. Lett.*, vol. 82, no. 4, p. 711, 1999.

[16] D. Hanneke, S. Fogwell, and G. Gabrielse, "New measurement of the electron magnetic moment and the fine structure constant," *Phys. Rev. Lett.*, vol. 100, no. 12, p. 120801, 2008.

[17] S. L. Zafonte and R. S. V. D. Jr, "Ultra-precise single-ion atomic mass measurements on deuterium and helium-3," *Metrologia*, vol. 52, no. 2, p. 280, 2015.

[18] S. Sturm, F. Koehler, J. Zatorski, A. Wagner, Z. Harman, G. Werth, W. Quint, C. H. Keitel, and K. Blaum, "High-precision measurement of the atomic mass of the electron," *Nature*, vol. 506, p. 467, 2014.

[19] H. A. Schuessler, E. N. Fortson, and H. G. Dehmelt, "Hyperfine structure of the ground state of ^{3}He$^+$ by the ion-storage exchange-collision technique," *Phys. Rev.*, vol. 187, pp. 5–38, Nov 1969.

[20] E. Fermi, "Über die magnetischen momente der atomkerne," *Zeitschrift für Physik*, vol. 60, pp. 320–333, May 1930.

[21] M. Bohman, A. Mooser, G. Schneider, N. Schoen, M. Wiesinger, J. Harrington, T. Higuchi, H. Nagahama, C. Smorra, S. Sellner, K. Blaum, Y. Matsuda, W. Quint, J. Walz, and S. Ulmer, "Sympathetic cooling of protons and antiprotons with a common endcap penning trap," *Journal of Modern Optics*, vol. 65, no. 5, p. 568, 2018.

[22] H. Nagahama, C. Smorra, S. Sellner, J. Harrington, T. Higuchi, M. Borchert, T. Tanaka, M. Besirli, A. Mooser, G. Schneider, K. Blaum, Y. Matsuda, C. Ospelkaus, W. Quint, J. Walz, Y. Yamazaki, and S. Ulmer, "Sixfold improved single particle measurement of the magnetic moment of the antiproton," *Nature Communications*, vol. 8, p. 14084, 2017.

[23] T. A. Savard, K. M. O'Hara, and J. E. Thomas, "Laser-noise-induced heating in far-off resonance optical traps," *Phys. Rev. A*, vol. 56, no. 2, p. R1095, 1997.

[24] A. Mooser, H. Kracke, K. Blaum, S. A. Bräuninger, K. Franke, C. Leiteritz, W. Quint, C. C. Rodegheri, S. Ulmer, and J. Walz, "Resolution of single spin flips of a single proton," *Phys. Rev. Lett.*, vol. 110, no. 14, p. 140405, 2013.

[25] C. C. Rodegheri, K. Blaum, H. Kracke, S. Kreim, A. Mooser, W. Quint, S. Ulmer, and J. Walz, "An experiment for the direct determination of the g -factor of a single proton in a penning trap," *New Journal of Physics*, vol. 14, no. 6, p. 063011, 2012.

[26] C. Smorra, A. Mooser, M. Besirli, M. Bohman, M. Borchert, J. Harrington, T. Higuchi, H. Nagahama, G. Schneider, S. Sellner, T. Tanaka, K. Blaum, Y. Matsuda, C. Ospelkaus, W. Quint, J. Walz, Y. Yamazaki, and S. Ulmer, "Observation of individual spin quantum transitions of a single antiproton," *Physics Letters B*, vol. 769, p. 1, 2017.

[27] A. Mooser, H. Kracke, K. Blaum, S. A. Bräuninger, K. Franke, C. Leiteritz, W. Quint, C. C. Rodegheri, S. Ulmer, and J. Walz, "Resolution of single spin flips of a single proton," *Phys. Rev. Lett.*, vol. 110, p. 140405, 2013.

[28] C. Smorra, K. Blaum, L. Bojtar, M. Borchert, K. Franke, T. Higuchi, N. Leefer, H. Nagahama, Y. Matsuda, A. Mooser, M. Niemann, C. Ospelkaus, W. Quint,

G. Schneider, S. Sellner, T. Tanaka, S. Van Gorp, J. Walz, Y. Yamazaki, and S. Ulmer, "Base – the baryon antibaryon symmetry experiment," *The European Physical Journal Special Topics*, vol. 224, p. 3055, Nov 2015.

[29] S. Ulmer, C. Smorra, A. Mooser, K. Franke, H. Nagahama, G. Schneider, T. Higuchi, S. V. Gorp, K. Blaum, Y. Matsuda, W. Quint, J. Walz, and Y. Yamazaki, "High-precision comparison of the antiproton-to-proton charge-to-mass ratio," *Nature*, vol. 524, p. 196, 2015.

[30] *Soft magnetic cobalt-iron alloys, Vacoflux and Vacodur.* `https://www.vacuumschmelze.de/fileadmin/Medienbiliothek_2010/Downloads/HT/PHT_004_CoFe.pdf`.

[31] C. de Carvalho Rodegheri, *Neuartige kryogene Penning-Falle für den Nachweis von Spin-Übergängen eines Protons und Bestimmung seines g-Faktors.* PhD thesis, Johannes Gutenberg-Universität Mainz, 2013.

[32] F. Koehler, K. Blaum, M. Block, S. Chenmarev, S. Eliseev, D. A. Glazov, M. Goncharov, J. Hou, A. Kracke, D. A. Nesterenko, Y. N. Novikov, W. Quint, E. M. Ramirez, V. M. Shabaev, S. Sturm, A. V. Volotka, and G. Werth, "Isotope dependence of the zeeman effect in lithium-like calcium," *Nature Communications*, vol. 7, no. 10246, 2016.

[33] A. Mooser, S. Braeuninger, K. Franke, H. Kracke, C. Leiteritz, C. Rodegheri, H. Nagahama, G. Schneider, C. Smorra, K. Blaum, Y. Matsuda, W. Quint, J. Walz, Y. Yamazaki, and S. Ulmer, "Demonstration of the double penning trap technique with a single proton," *Physics Letters B*, vol. 723, no. 1, p. 78, 2013.

[34] COMSOL Multiphysics ® v. 5.3.a `www.comsol.com`. COMSOL AB, Stockholm, Sweden.

[35] S. Ulmer, *First Observation of Spin Flips with a Single Proton Stored in a Cryogenic Penning Trap.* PhD thesis, Ruperto-Carola University of Heidelberg, 2011.

[36] G. Schneider, *300 ppt Measurement of the Proton g-Factor.* PhD thesis, Johannes Gutenberg-Universität Mainz, 2017.

[37] R. Rejoub, B. G. Lindsay, and R. F. Stebbings, "Determination of the absolute partial and total cross sections for electron-impact ionization of the rare gases," *Phys. Rev. A*, vol. 65, p. 042713, Apr 2002.

[38] M. B. Shah, D. S. Elliott, P. McCallion, and H. B. Gilbody, "Single and double ionisation of helium by electron impact," *Journal of Physics B: Atomic, Molecular and Optical Physics*, vol. 21, pp. 2751–2761, aug 1988.

[39] F. L. Moore, *High Resolution Mass Spectrometry in Quadring Penning Trap.* PhD thesis, University of Washington, 1989.

[40] "Alfa aesar titanium foil." `https://www.alfa.com/de/catalog/010398/`.

[41] "Alfa aesar titanium sponge." `https://www.alfa.com/en/catalog/042459/`.

[42] "Indirect, gas-dependent pressure measurement." `https://www.pfeiffer-vacuum.com/en/know-how/vacuum-measuring-equipment/fundamentals-of-total-pressure-measurement/indirect-gas-dependent-pressure-measurement/`.

[43] P. R. F. A. Paneth and K. I. Mayne, "Production by cosmic rays of helium-3 in meteorites," *Nature*, vol. 172, p. 200, 1953.

[44] F. J. Norton, "Permeation of gases through solids," *Journal of Applied Physics*, vol. 28, no. 1, pp. 34–39, 1957.

[45] D. E. Swets, R. W. Lee, and R. C. Frank, "Diffusion coefficients of helium in fused quartz," *The Journal of Chemical Physics*, vol. 34, no. 1, pp. 17–22, 1961.

[46] M. Redshaw, A. L. Benjamin, G. Bollen, R. Ferrer, D. L. Lincoln, R. Ringle, S. Schwarz, and A. A. Valverde, "Fabrication and characterization of field emission points for ion production in penning trap applications," *International Journal of Mass Spectrometry*, vol. 379, pp. 187 – 193, 2015.

[47] A. A. Wagner, *The g-factor of the valence electron bound in lithiumlike silicon $^{28}Si^{11+}$: The most stringent test of relativistic many-electron calculations in a magnetic field.* PhD thesis, Ruperto-Carola University of Heidelberg, 2013.
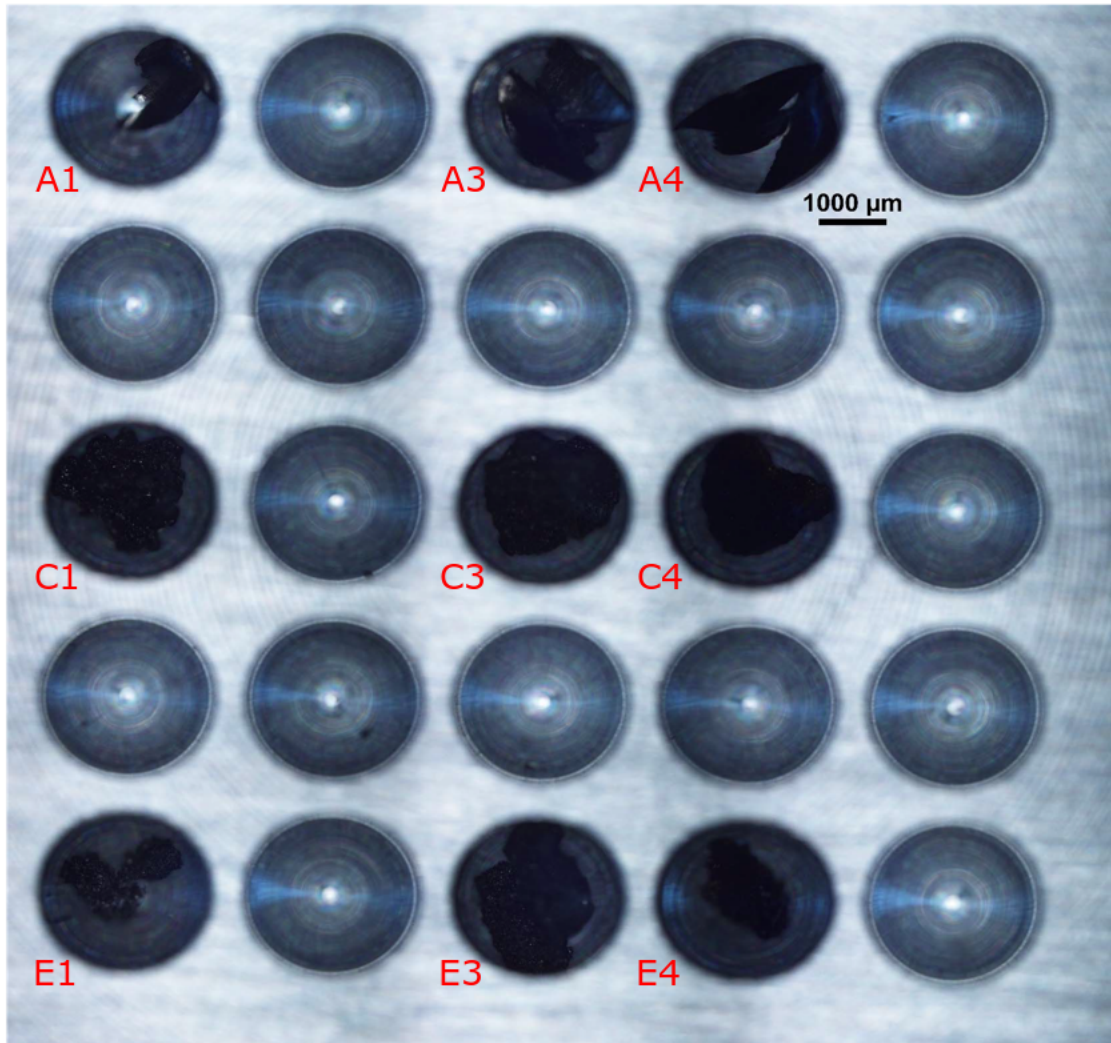
B Titanium Sample Photographs

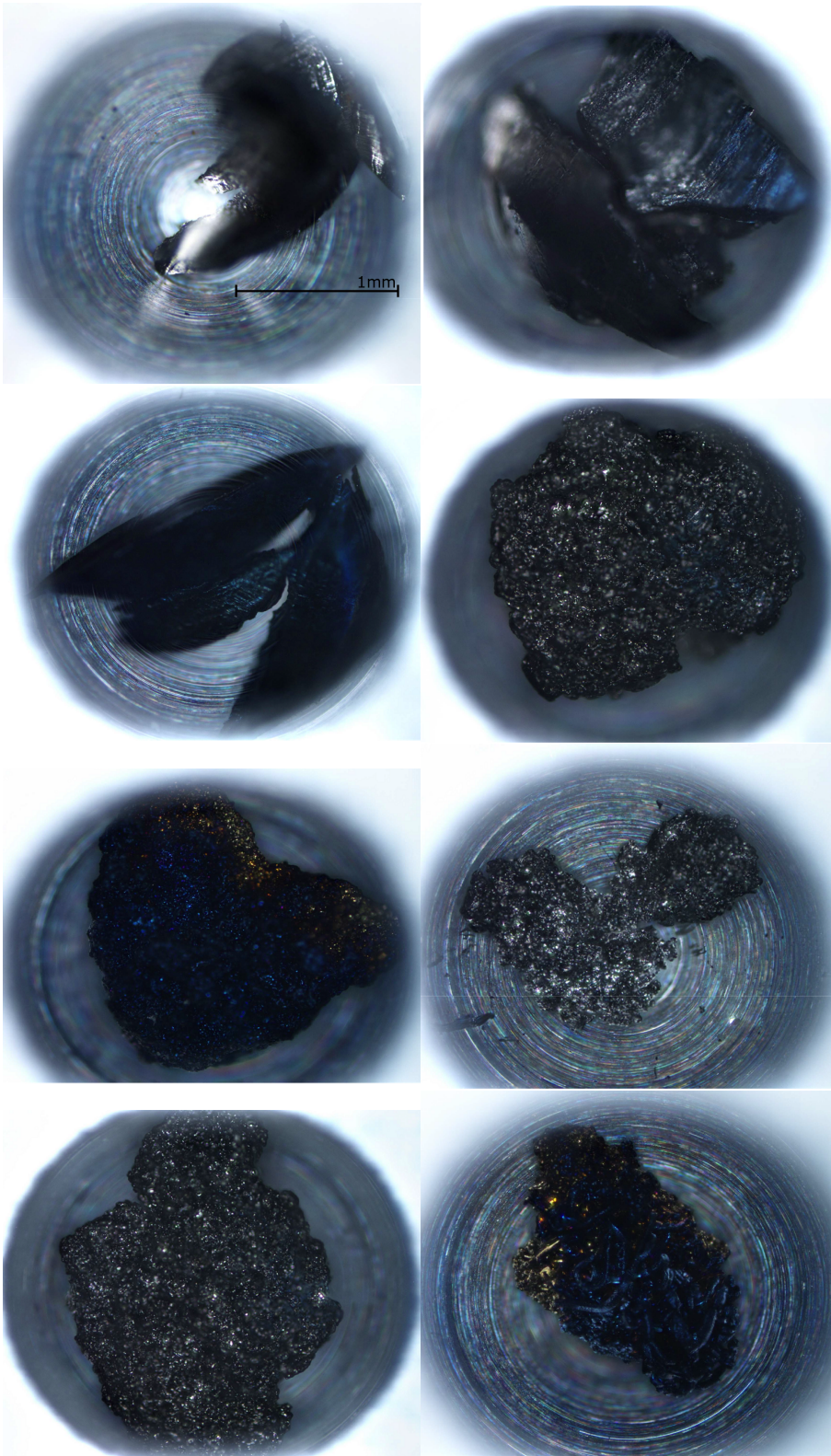Figure B.1: Loaded sample holder of the first measurement before melting

Figure B.2: From top left to bottom right: samples A1, A3, A4, C3, C4, E1, E3 and E4 before melting
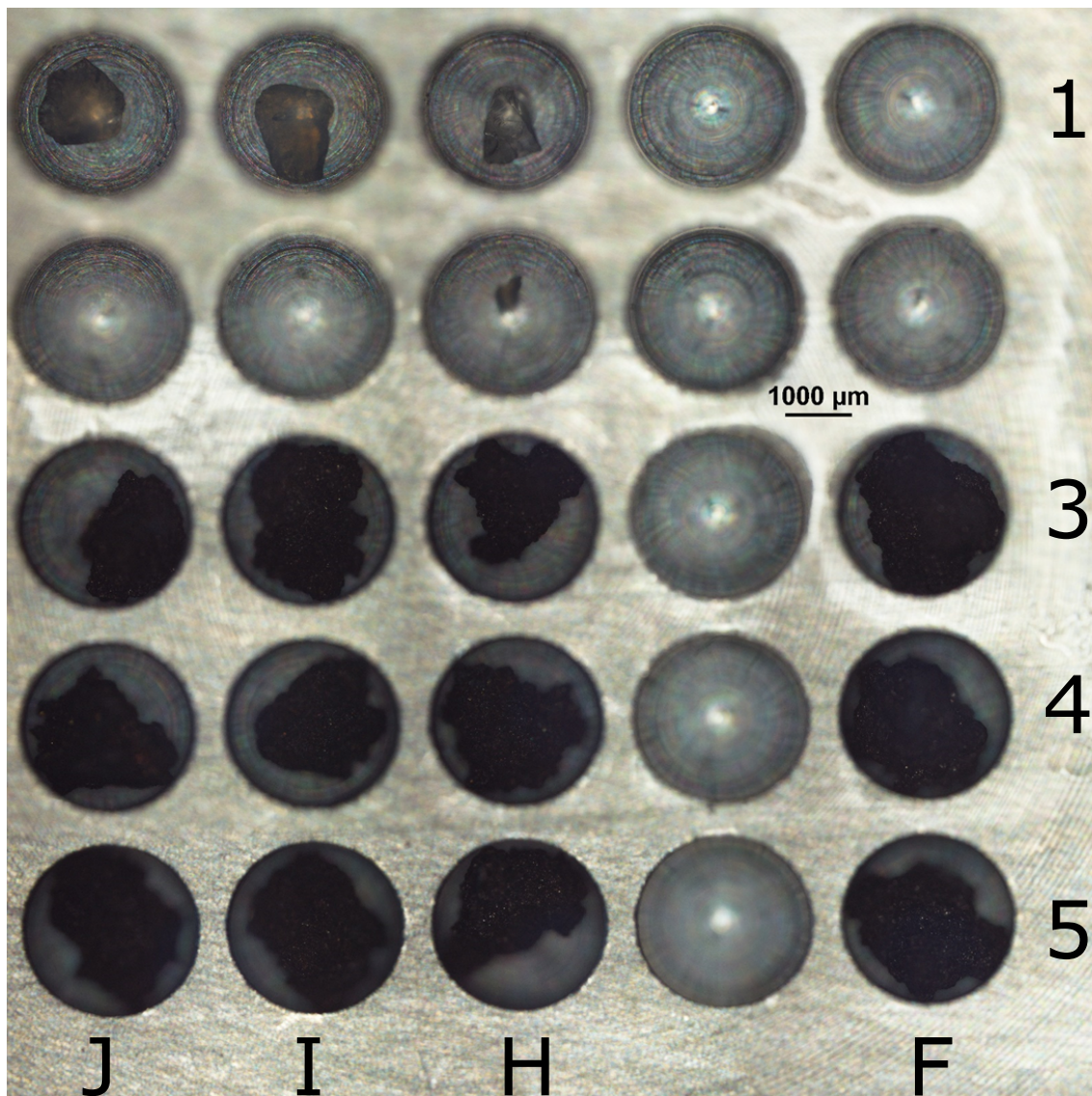
Figure B.3: Samples tested in the second measurement before melting. In row 1 also three airogel samples were added, which were found to contain no measurable amount of helium after one week in room temperature.
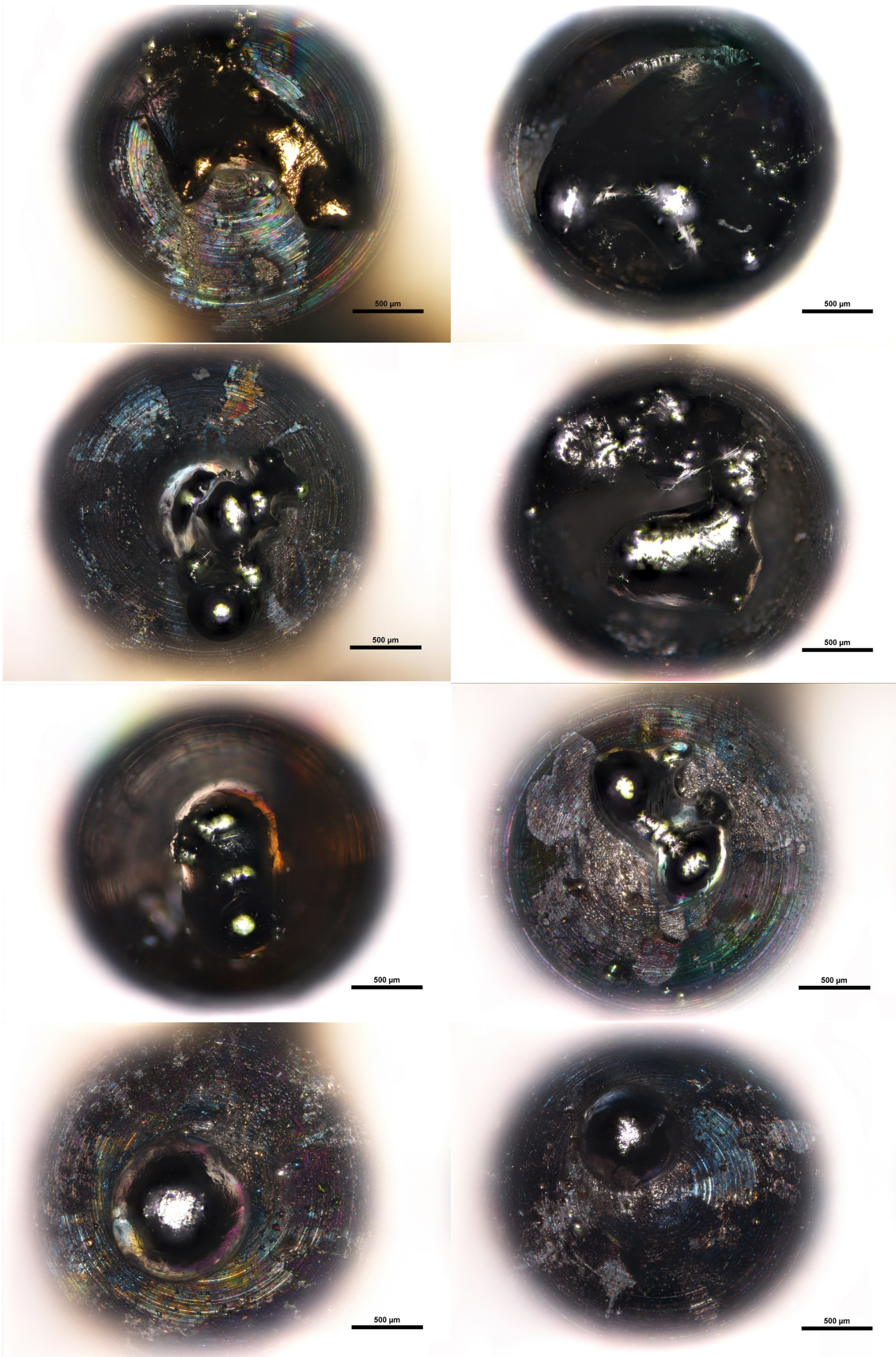
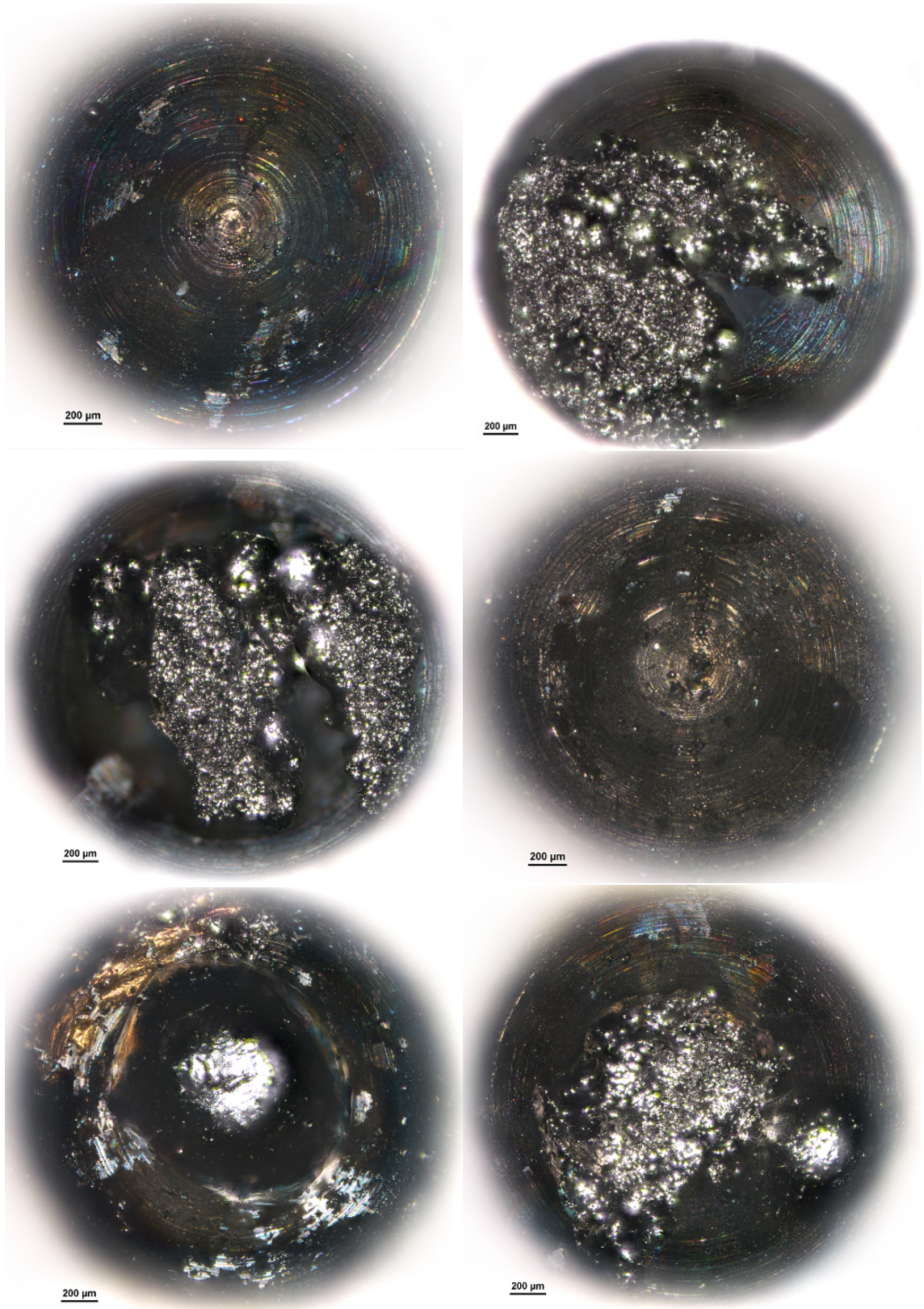Figure B.4: From top left to bottom right: samples A1, A3, C1, C3, C4, E1, E3 and E4 after melting

Figure B.5: From top left to bottom right: samples F3, F5, H3, H4, H5 and I3 after melting
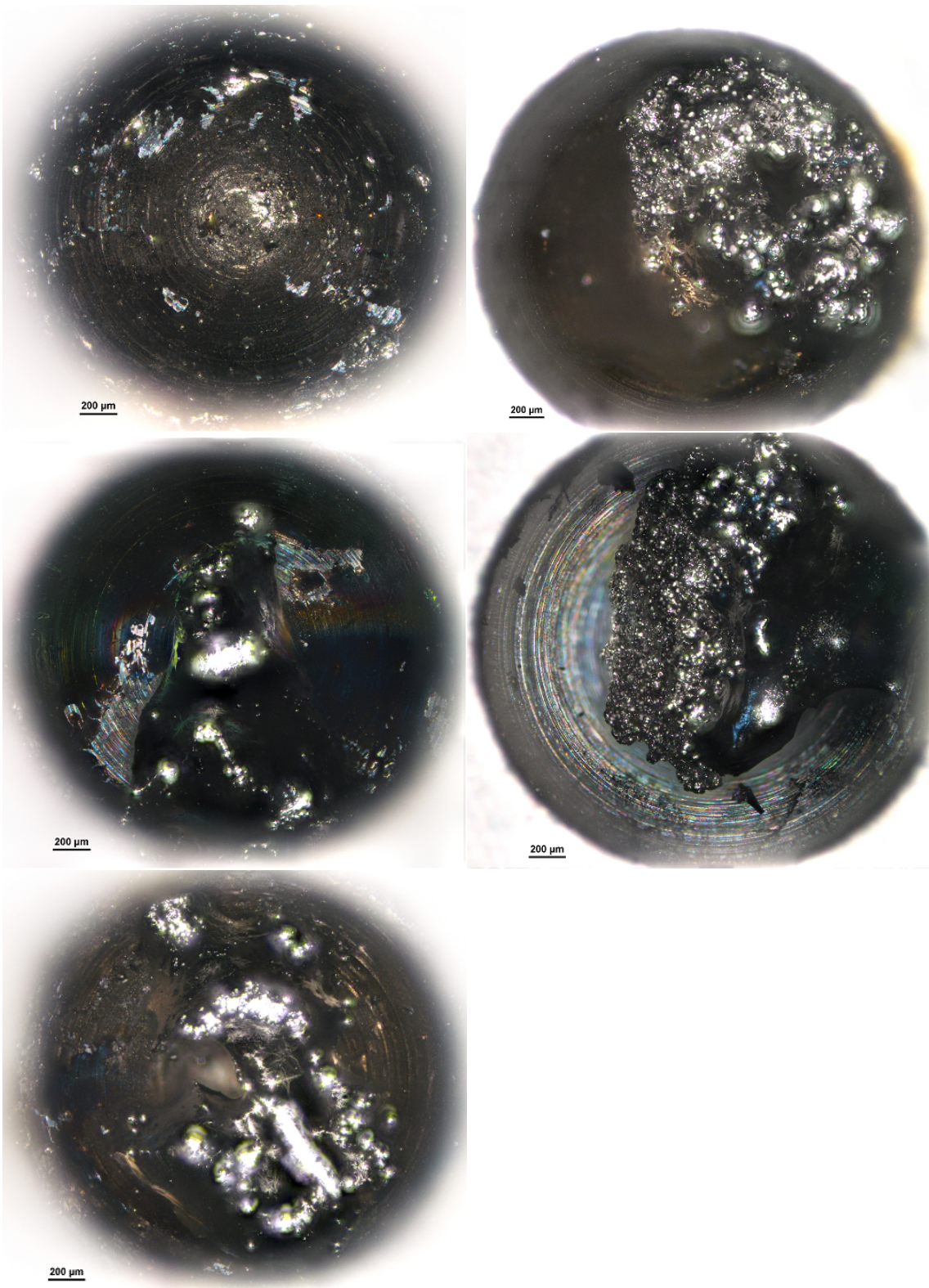
58

Figure B.6: From top left to bottom right: samples I4, I5, J3, J4 and J5 after melting

Erklärung:

Ich versichere, dass ich diese Arbeit selbstständig verfasst habe und keine anderen als die angegebenen Quellen und Hilfsmittel benutzt habe.

Heidelberg, den (Datum)   . . . .